Choroid Plexus Hosts the Earliest Detectable Circadian Clock in the Brain

Hélène Vitet [1], Vuong Hung Truong [1], Jihwan Myung [1,2,*]

[1] Laboratory of Braintime, Graduate Institute of Mind, Brain and Consciousness (GIMBC), Taipei Medical University, New Taipei City 235, Taiwan
[2] Graduate Institute of Medical Sciences (GIMS), College of Medicine, Taipei Medical University, Taipei 110, Taiwan

[*] Correspondence: Jihwan Myung (jihwan@tmu.edu.tw)

Abstract

Embryonic circadian rhythms support normal development, and maternal chronodisruption is linked to miscarriages and neurodevelopmental risk, yet the identity of the earliest brain circadian oscillator and the mechanisms governing its emergence remain unknown. Using bioluminescent reporters for *Per2* and *Bmal1*, we identified the developmental window in which autonomous ~24 h oscillations first appear *ex vivo*. Contrary to the prevailing view that places the suprachiasmatic nucleus (SCN) as the earliest circadian structure at E14.5–E15.5, we found that the fourth ventricle choroid plexus (4VCP) exhibits PER2::LUC oscillations by E11.5–E12.5. Transcriptional profiling revealed significant phase shifts in multiple clock genes between E11.5 and E13.5, indicating a transition away from maternal synchrony and the onset of a differentiation program. Detailed characterization of these early oscillations revealed hallmarks consistent with a saddle-node on an invariant circle (SNIC) bifurcation. Our findings establish the 4VCP as the earliest detectable brain circadian oscillator and clarify the process leading to the onset of the embryonic circadian clock in the brain. These results provide insights into maternal and fetal clock interactions during development, with potential implications for neonatal care.

Keywords: circadian clocks, choroid plexus, embryonic development, SNIC bifurcation, clock emergence, maternal synchrony

Graphical Abstract:

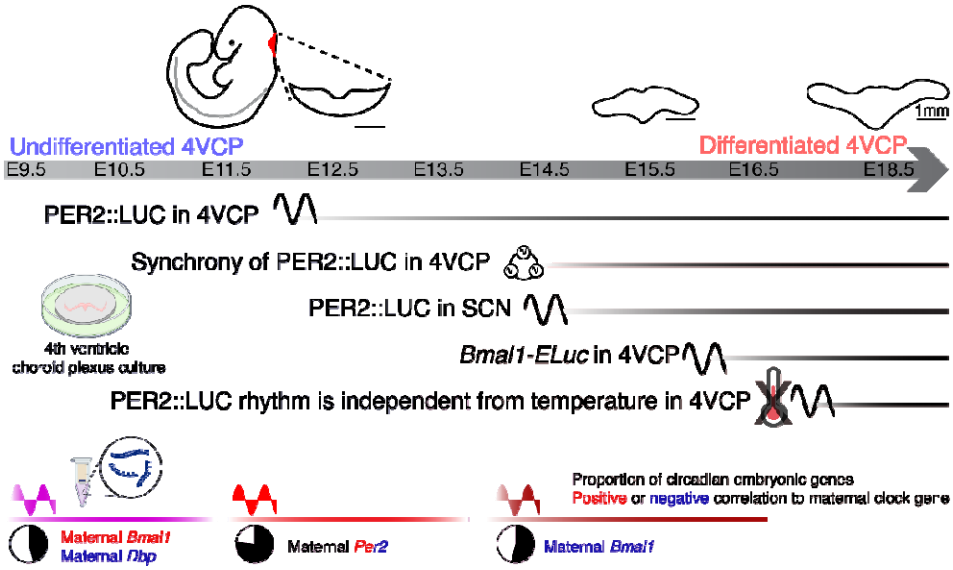

Timeline of 4VCP clock emergence before the SCN. In the embryonic 4VCP, PER2::LUC oscillations appear at E11.5–E12.5, and cellular synchrony increases abruptly around E14.5. *Bmal1-ELuc* oscillations appear at E13.5. The 4VCP entrains to a 0.5 °C temperature cycle through E16 but not at E18. The lower pie charts and gradients summarize the fraction of embryonic clock genes that are circadian and their correlation with maternal *Bmal1*, *Dbp*, and *Per2* expression.

Introduction

Circadian clocks are fundamental pacemakers that align physiology with the 24 h rhythms of Earth. Physiological processes occur within a circadian timescale autonomously maintained by the transcription-translation feedback loop (TTFL). In this loop, the positive feedback component BMAL1:CLOCK activates transcription of the core negative feedback components such as *Per* and *Cry*, and the resulting PER:CRY complexes accumulate with a delay before repressing their own transcription upon translocation. While most mammalian tissues express circadian clocks, the suprachiasmatic nucleus (SCN) in the hypothalamus acts as the central clock, synchronizing other clocks throughout the body. Although mature circadian systems are increasingly well characterized, the timing and locus of the emergence of circadian rhythms during development remain poorly defined.

When? Circadian rhythms have been observed in prenatal stages in humans, non-human primates, and rodents (Maeda et al., 2006; Serón-Ferré et al., 2012; Landgraf et al., 2014). However, detecting embryonic clocks presents technical challenges, as experimental findings are often inconsistent due to low-amplitude oscillations and tissue-specific differences in clock gene expression. Although *Per* and *Bmal1* did not show clear rhythms when measured in whole-embryo *ex vivo* preparations (E10 to E17) (Cao et al., 2022; Dolatshad et al., 2010; Serón-Ferré et al., 2012), the circadian rhythmicity of PER2 has been detected in the SCN *ex vivo* around E14.5 to E15.5 (Wreschnig et al., 2014; Carmona-Alcocer et al., 2018) and around E18 in peripheral organs such as the kidney (Dan et al., 2020), the heart (Umemura et al., 2017), and the liver (Dolatshad et al., 2010).

Embryonic brain morphogenesis depends on a complex interplay between the neural tube and the cerebrospinal fluid pressure gradients. The dynamic homeostasis of cerebrospinal fluid (CSF), produced primarily by the choroid plexus (CP), must be tightly regulated during this process. This non-neuronal tissue performs two roles: the CP filters the blood through its epithelial cells to produce CSF, acting as a gatekeeper at the fluid boundary of the brain, and it releases signaling molecules (5-HT, miRNAs) as well as peptides and proteins (TTR, cytokines, IGF2) into the CSF to support processes such as metabolism and signal transduction (Saunders et al., 2023; Chau et al., 2015; Courtney et al., 2025; Edelbo et al., 2023). In the embryo, the onset timing of CP epithelial CSF production remains unclear, in part because early in development the CP is not the only structure that modulates CSF composition (Bueno et al., 2020; Parvas et al., 2008). CSF is present as early as neural tube closure at E9.5, initially derived from the enclosed amniotic fluid. Its composition then transitions to CP-produced fluid between E10.5 and E14.5, coinciding with CP formation (Chau et al., 2015).

Where? Little is known about the exact locus in the brain where the earliest circadian clock emerges. Using bioluminescent reporters of circadian gene expression, PER2::LUC and *Bmal1-ELuc*, we scanned *ex vivo* brain slices for circadian oscillations and monitored tissue explants collected from E9.5 onward throughout embryogenesis. This screening identified the 4VCP as the earliest locus with detectable circadian clock oscillations. We recently found that, in adult mice, the CP acts as a strong clock, as indicated by the persistence and amplitude of PER2::LUC reporter oscillations and by its ability to entrain the SCN (Myung et al., 2018). The CP is present in each of the brain ventricles, which are filled

with the CSF. The lateral ventricle CP (LVCP) is contiguous with the third ventricle CP (3VCP) and separate from the fourth ventricle CP (4VCP) in the hindbrain. Differences among CPs include their developmental timelines and transcriptomes (Saunders et al., 2023; Lun et al., 2015a; Dziegielewska et al., 2001). In mice, the 4VCP develops first, followed by the LVCP (Lun et al., 2015b). Arising from the lower rhombic lip, between the roof plate and dorsal neuroepithelium, 4VCP development begins as early as E9.5, when it expresses *Wnt1*, transthyretin (*Ttr*), and potassium voltage-gated channel subfamily E member 2 (*Kcne2*). Development peaks between E11 and E12.5 (Lun et al., 2015b; Hunter and Dymecki, 2007), after which the 4VCP becomes anatomically apparent and is thought to be complete by E14, although proliferation continues postnatally (Lun et al., 2015b). At this stage, 4VCP cells are mature and express *Ttr, Otx2,* and *Wnt5a*, among other genes.

Embryonic CSF is crucial for the survival, proliferation, and differentiation of neural progenitors (Miyan et al., 2003; Martin et al., 2009; Gato et al., 2005; Parada et al., 2008; Alonso et al., 2011 and 2017; Huang et al., 2009) by delivering peptides and molecules, such as morphogens (retinoic acid, Sonic Hedgehog) and growth or trophic factors, such as FGF2 (Martin et al., 2006), EGF (Birecree et al., 1991), and IGF (Zappaterra and Lehtinen, 2012). CSF is also known for its role in shaping the brain through pressure against neuroepithelial walls (Gato and Desmond, 2009). The strong clock in the CP is thought to regulate this CSF secretome, which is sensitive to time of the day (Edelbo et al., 2023). Very recently, apocrine secretion from the CP to the CSF has been identified as a cause of neuronal progenitor stimulation and offspring behavior modification (Courtney et al., 2025). However, the embryonic CP clock remains poorly characterized, although it could modulate the temporal composition of CSF and, consequently, neurogenesis.

How? Circadian clocks are present across many mammalian cell types (Balsalobre et al., 1998; Yamazaki et al., 2000; Yoo et al., 2004), yet the locus-specific sequence of its emergence in the brain suggests a programmed onset of circadian oscillations (Wreschnig et al., 2014; Carmona-Alcocer et al., 2018). Developmentally, the early embryo operates on distinct timescales, with cell divisions occurring on the order of hours before lengthening during neurogenesis, and somitogenesis proceeding on a short timescale of hours (Caviness et al., 1995; Oates et al., 2012). These rhythms may not synchronize well with the circadian clock, especially as the cell division timescale changes gradually. An abrupt transition between the somitogenesis era and the circadian era has been proposed (Yagita *et al.*, 2024), making the sudden emergence of the circadian clock *in vivo* plausible.

In nonlinear dynamics, a stable equilibrium can transition to a stable oscillation through mechanisms called bifurcations (Strogatz, 2024). Several types of bifurcation are distinguished by how amplitude and period behave near threshold and by their robustness to perturbations. Many oscillating biological systems, including circadian oscillators, are described by a (supercritical) Hopf bifurcation, characterized by a gradual increase in oscillation amplitude while the period stays near 24 h. The Hopf-based oscillator often fits dynamics of circadian clocks, consistent with experimental and modeling work (Murayama et al., 2017; Battogtokh and Tyson, 2018). Similarly, adult sinoatrial node pacemaking is typically governed by Hopf-type mechanisms, whereas the developmental onset of the first heartbeat in zebrafish arises via a noisy SNIC bifurcation (Jia et al., 2023). The saddle-node on an

invariant circle (SNIC), also called SNIPER, is characterized by the abrupt appearance of nonzero amplitude and an initially long period that shortens toward ~24 h. At the single-cell level in the 4VCP, we observe a near-step increase in amplitude at onset and a progressive shortening of period over development, hallmarks consistent with SNIC-type dynamics. This bifurcation has specific implications in maternal-fetal coupling. Near a SNIC threshold, slow dynamics make oscillation frequency highly sensitive to weak biases. Consequently, weak maternal cues can efficiently entrain the nascent CP clock and synchronize weakly coupled CP cells by common drive. We observed such behavior at E14 in *ex vivo* 4VCP explants subjected to low-amplitude rhythmic temperature input.

In this study, we pinpoint when circadian rhythms first emerge in the 4VCP, identifying it as the earliest detectable clock in the embryonic mouse brain. We find hallmarks consistent with discrete appearance of the circadian clock, including SNIC-like bifurcation behaviors and abrupt synchronization over development. These results clarify the timing, locus, and onset dynamics of the brain's first clock that potentially governs fluid homeostasis and suggest implications for maternal chronodisruption, including shift work, during early pregnancy that can elevate risks of miscarriages and preterm birth (Cai et al., 2019; Davari et al., 2018), and for circadian support in neonatal care settings such as the Neonatal Intensive Care Unit (NICU) where preterm infants often show impaired rhythmicity (Govindan et al., 2024).

Material and Methods

Mice

Homozygous PER2::LUC mice (B6.129S6-*Per2*^{tm1Jt}/J, RRID: IMSR_JAX:006852) and heterozygous *Bmal1-ELuc* mice (Nakajima et al., 2010; a gift from Daisuke Ono, Nagoya University), maintained on the C57BL/6J background, were crossed with wild-type C57BL/6J animals to generate heterozygous PER2::LUC$^{+/-}$ or *Bmal1-ELuc*$^{+/-}$ embryos. The PER2::LUC fusion protein reporter tracks PER2 abundance through a luciferase reaction (Yoo et al., 2004). *Bmal1* transcriptional activity was monitored with the *Bmal1-ELuc* reporter, with high baseline removed through Hodrick-Prescott filter-based detrending (Myung et al., 2012). In this study, we treat *Bmal1-ELuc* as a transcript-level proxy and PER2::LUC as a protein-level proxy, as its luciferase activity peaks several hours after *Per2* transcription (Myung et al., 2025). Both females and males were maintained under equinox light-dark (LD) cycles (12 h light:12 h dark; lights on at 07:00 and off at 19:00), with light-dark schedules controlled by LocoBox software (Truong and Myung, 2023) and constant ambient temperature and humidity conditions (24.0 ± 1.8°C; 50.2 ± 8.7% RH). For sampling at ZT14 and ZT20, we used a reverse dark-light (DL) cycle (lights on at 22:00 and off at 10:00) and validated that gene expression levels matched those under LD cycles at E13.5 (**Fig. S1**). All animal protocols were reviewed and approved by the Institutional Animal Care and Use Committee (IACUC) of Taipei Medical University Laboratory Animal Center (protocols LAC-2019-0430, LAC2022-0381, LAC2022-0477, LAC2023-0037, and LAC2023-0038).

Tissue isolation and explant culture

165 ***Direct dissection.*** Tissue culture and bioluminescence recording protocols were identical to those used
166 previously (Myung et al., 2018). Pregnant female mice were anesthetized with isoflurane and
167 euthanized at defined Zeitgeber times, and brains and embryos were rapidly removed into ice-cold
168 Hank's balanced salt solution (HBSS; Sigma-Aldrich), supplemented with penicillin-streptomycin
169 (10,000 U/mL; Gibco) and HEPES (1 M, pH 7.4). Embryonic tissues were dissected after decapitation
170 using forceps and a scalpel under a stereomicroscope. For E9.5, the prosencephalon (containing both
171 the SCN and LVCP progenitors) and the rhombencephalon (containing the 4VCP progenitors) were
172 collected. For E10.5–E12.5, the 4VCP was extracted from the inferior part of the hindbrain roof plate
173 epithelium, i.e., the lower rhombic lip containing rhombomere 2-8, located between the otic vesicles
174 and the posterior part of rhombomere 1 (Hunter and Dymecki, 2007). For the LVCP, the cortical midline
175 was considered to host the LVCP progenitors. After E12.5, the CP becomes clearly distinguishable, and
176 its dissection is similar to that of the adult mouse. The precision of 4VCP isolation throughout
177 development was validated by RT-qPCR (**Fig. S2**). The SCN from E10.5 to E13.5 was dissected from the
178 ventral hypothalamus between the two optic cups (developing eyes). After E13.5, the SCN and the optic
179 chiasm become more distinct, and the dissection procedure is the same as in the adult. This protocol
180 was also used to isolate maternal and embryonic tissues in ice-cold PBS for biomolecular experiments.
181
182 ***Placenta dissection.*** We separated the light pink outer layer of the placenta (maternal decidua,
183 considered here as the maternal placenta) from the darker pink inner layer (junctional zone and
184 labyrinth, considered here as the embryonic placenta). The weak junction between these two sides of
185 the placenta allows dissection with tweezers.
186
187 ***Tissue slicing.*** Heads or brains of mouse embryos at E11.5, E13.5, or E15.5 were sliced *ex vivo* on a
188 vibratome (VT1000S, Leica Biosystems). Tissue was briefly dipped in two successive baths of low-
189 melting point agarose (2% w/v; CAS 9012-36-6) at 37 °C, then embedded in an agarose block, glued to
190 the vibratome stage and immersed in ice-cold HBSS. Using a diamond blade (Delaware Diamond
191 Knives) advancing at ~0.025 mm/s and maximum frequency, 300 µm-thick slices were made and
192 transferred to a culture membrane.
193
194 ***Explant culture.*** Each explant was cultured on a culture membrane insert (PICM0RG50, Merck
195 Millipore) in a 35-mm dish containing 1 mL DMEM (Sigma-Aldrich) supplemented with B-27 (Gibco) and
196 200 µM beetle luciferin (Promega). The dish lid was sealed with high-vacuum grease (Molykote,
197 DuPont) to prevent evaporation and maintained at a constant temperature of 37.00 ± 0.01°C in a
198 hybrid refrigerator-heater incubator (MIR-154-PA, PHCbi). Temperature was monitored by placing an
199 iButton (DS1921L, Maxim Integrated) adjacent to the dishes.
200
201 **iDISCO tissue clearing and immunofluorescence labeling**

202 After culture, the membrane supporting the brain slices was cut out and cleared using the iDISCO
203 protocol (https://idisco.info/idisco-protocol). Briefly, after fixation in 4% PFA, the slices were rinsed and
204 incubated in PBS for 3 days, then dehydrated in MeOH/H_2O in micro glass vials with PTFE caps,
205 followed by an overnight incubation in 66% DCM/33% MeOH. Samples were then washed and bleached

206 in 5% H_2O_2 overnight, before being rehydrated in MeOH/H_2O. Immunolabelling was conducted in a 96-
207 well plate, starting with permeabilization (1 day) and blocking (1 day) at 37°C, followed by incubation
208 with primary antibody TTR (AB_10723946; GTX85112, chicken, 1:500, Genetex) for 2 days at 37°C. Slices
209 were then washed and incubated with secondary antibody (anti-chicken Alexa Fluor 568; AB_175477;
210 ab175477, goat, 1:1000, Abcam) for 2 days at 37°C. Similar steps of wash and blocking were applied
211 before consecutive incubations with LHX1 (AB_531784; 4F2-c, mouse, 1:500, DSHB) and anti-mouse
212 CF350 (SAB4600222, goat, 1:1000, Sigma) as before. Slices were then transferred back to the micro
213 glass vials to undergo final clearing, beginning with dehydration in MeOH/H_2O followed by a 3-h
214 incubation in 66% DCM/33% MeOH at room temperature. Finally, two 15 min incubations in 100% DCM
215 were performed before mounting the slices on glass slides. DBE was added directly over the slices,
216 confined under a coverslip, and sealed with nail polish. Slices were then imaged using a DM IL
217 fluorescence microscope (Leica Microsystems).
218
219 **Time-lapse bioluminescence luminometry and imaging**

220 ***Bioluminescence luminometry.*** For luminometry, the overall bioluminescence from each sample was
221 recorded every 15 min with an integration time window of 108 s per dish, using a 32-dish rotating wheel
222 with four photon-counting photomultiplier tubes (PMTs) (LumiCycle 32, Actimetrics), housed in a
223 refrigerator-heater incubator for precise temperature control (MIR-154-PA, PHCbi). Temperature was
224 recorded continuously throughout the experiment.
225
226 ***Bioluminescence imaging.*** Single-cell imaging was performed on a custom-built incubator-microscope
227 system equipped with the Orca R2 cooled CCD camera (Hamamatsu) with water cooling, combined
228 with a 4x, NA 0.16 objective (UPLXAPO, Olympus) coupled to a 0.35x reduction lens (U-TV0.35XC-2,
229 Olympus) to increase photon collection from bioluminescence (Myung et al., 2024), with a stage-top
230 incubator (INUG2-WELS, Tokai Hit). Binning was set to 4×4, and exposure time was 60 min. Images
231 were acquired using Micro-Manager 1.4 (Vale Lab, UCSF) via the DCAM-API (Hamamatsu) driver.
232
233 **Real-time quantitative qPCR (RT-qPCR)**

234 ***RNA Isolation, cDNA synthesis, and RT-qPCR.*** After dissection of the embryonic or maternal 4VCPs at
235 ZT2, ZT8, ZT14, and ZT20, the samples were stored at -80°C. Embryonic 4VCPs from one dam (3-11
236 embryos per litter) were pooled, and at least 2-3 litters per time point were used. RNA sampling and RT-
237 qPCR methods followed our previous protocol (Myung et al., 2015). 300 µL of TRK lysis buffer
238 containing 2% β-mercaptoethanol was added to each sample, followed by an equal volume of
239 chloroform after intensive homogenization. After phase separation and ethanol addition,
240 microcolumns from the ENZA MicroElute Total RNA Kit (Omega Bio-Tek) were used to collect total
241 RNA, with a final elution volume of 21 µL in DEPC-treated water. After evaluating the RNA
242 concentration, cDNA was synthesized from 0.5–1 µg of total RNA using SuperScript IV Reverse
243 Transcriptase (Thermo Fisher Scientific) with oligo$(dT)_{20}$ primers. PowerUp SYBR Green Master Mix
244 (Applied Biosystems) was added to the cDNA samples, and RT-qPCR was performed in technical

245 triplicate on a QuantStudio 3 Real-Time PCR System (Thermo Fisher Scientific). Primer sequences
246 tested and used are listed in **Table S1**.
247
248 ***Normalization.*** *Gapdh*, *Actb* (*β-actin*), and *Rpl13a* served as internal controls for embryonic samples
249 (Hildyard et al., 2022). G*apdh* and *Actb* were used for maternal samples. For embryonic samples,
250 differentiation status of each gene was assessed as the relative abundance of mRNA at a given
251 embryonic stage ($n > 8$) normalized to the maximum abundance observed between E9.5 and E16.5. For
252 example, at E9.5:

253 $$RNA_{E9.5}\,(\%) = \frac{mean\ (RNA_{E9.5})}{max\ (RNA_{E9.5-E16.5})} \times 100 \qquad (1)$$

254
255 **Spectral analysis of bioluminescent time series and time of emergence quantification**

256 ***Preprocessing.*** Visualization and preprocessing, including periodogram and fast Fourier transform
257 (FFT)-based spectral analysis, were performed on Mathematica 13 (Wolfram Research) using the
258 custom PMTAnalysis package (http://sourceforge.net/projects/imaginganalysis). Before analysis, the
259 first 6 h of each recording were truncated. All circadian periods of the bioluminescence oscillations were
260 estimated using FFT, and amplitudes were quantified as the root mean square (RMS) of detrended
261 oscillations over fixed analysis windows: nominally 7 days for luminometry and 4VCP imaging, and 4
262 days for whole brain slice imaging. Because the first 6 h were removed, some recordings were slightly
263 shorter than 7 days. For image analysis of brain slices or the 4VCP, a 2×2-pixel grid was applied to the
264 time-lapse images after removal of outlier pixels, and each ROI's standard deviation, center of mass,
265 and mean gray value were measured using ImageJ (NIH).
266
267 ***Circadian power.*** Using a sliding-window FFT (2-day for luminometry data and 3-day for imaging data),
268 the time-lapse bioluminescence signals from PER2::LUC or *Bmal1-ELuc* were decomposed into spectral
269 power and visualized as spectrograms over time. After integrating the power within specific period
270 bands, the circadian power was calculated as the ratio of the total power in the circadian range (24 ± 4
271 h) to the total power across the full period range (3–58 h) (**Fig. S3**). This yielded a time series of percent
272 circadian power, which quantifies how strongly a gene oscillates within the circadian band relative to
273 other period bands. Finally, the overall circadian power was computed as the average of these window-
274 wise circadian power values across the entire recording. Circadian power thus provides a metric that
275 captures the robustness of the circadian rhythm and accounts for damping, period variability, and
276 noise. For a perfect sinusoid in a 2-day window, the maximal circadian power reaches ~60%, whereas
277 for transient, rapidly damped oscillations, it falls below 20% (**Fig. S3**). The blank control (luciferase
278 medium without tissue explant) showed a maximal circadian power of ~20% (n=10) (**Fig. 2D**). For SCN
279 and 4VCP explants, the half-maximal level of the fitted circadian power curve across development was
280 ~30% (30.83 ± 2.36% and 31.28 ± 1.70%, respectively).
281
282 ***Emergence Time.*** For rigorous identification of the emergence time points of the PER2::LUC and
283 *Bmal1-ELuc* circadian rhythms, we performed nonlinear curve fitting using a sigmoid function. Blank

recordings were used to estimate baseline circadian power and to provide null data points prior to E9.5. We then defined the emergence time (T_e) as the time when one-half of the maximum circadian power was reached (eq. 2).

$$P(t) = \frac{A}{1+e^{-(t-T_e)/\tau)}} + C_0 \qquad (2)$$

where $P(t)$ is the circadian power at time t (time of sampling for explant), A is the amplitude above baseline, T_e is the half-maximal emergence time, τ is the time constant (slope parameter), and C_0 is the baseline determined from blank recordings, with maximal power given by $A + C_0$.

Hierarchical clustering and spectral analysis of qPCR gene expression profile

Hierarchical clustering. To ensure comparability across genes, expression levels were first normalized using the internal control genes, then standardized using Z-scores: for each gene, the mean normalized expression was subtracted from each time point and the result was divided by the standard deviation across all time points. To explore temporal relationships between genes, we used hierarchical clustering as implemented in the seaborn.clustermap function (v0.11.2) in Python (v3.6.13). This function computes pairwise distances between gene expression profiles using the Pearson correlation r_{ij} as the distance metric between genes i and j. Clustering was performed using average linkage, and results were visualized as a cluster heat map with a dendrogram that represents the similarity relationships among genes based on their temporal patterns. Average linkage distance $D(A, B)$ was calculated as:

$$D(A, B) = \frac{1}{m\,n} \sum_{i \in A} \sum_{j \in B} d(i, j) \qquad (3)$$

where m and n are the numbers of genes in clusters A and B, respectively, and $d(i, j)$ is the distance (1 - r_{ij}) between genes i and j. To summarize clusters, we identified representative genes for each cluster. For a given cluster, we computed its centroid by averaging the Z-scored expression profiles of all member genes across time points. We then calculated the Pearson correlation between each gene in the cluster and the cluster centroid. The gene with the highest correlation to the centroid was designated as the representative gene for that cluster, as it best reflected the average temporal pattern of its cluster.

Synchrosqueezed continuous wavelet transform (SST-CWT). Circadian gene expression profiles in embryos are sparsely sampled, and conventional Fourier or continuous wavelet transforms (CWT) often yield broad, smeared power spectra when signals have non-stationary components. SST-CWT sharpens time-frequency estimates by reassigning CWT coefficients from a range of supporting frequencies to a more precise instantaneous frequency (Daubechies et al., 2011). We implemented SST-CWT using the cwt_sst function from the squeezepy library (v0.6.5; https://github.com/OverLordGoldDragon/ssqueezepy). Prior to analysis, normalized gene expression time series were detrended with a moving average filter to reduce baseline drift. The signal was then mirrored and extended to improve edge behavior during the wavelet transform. We used a Morlet wavelet and 90 voices per octave. Although SST-CWT yields an amplitude spectrum, we refer to it here as a "power spectrum" to align with common usage in circadian biology (true power can be obtained by

squaring the amplitude). From the SST-CWT output, we retained periods from 3 to 58 h and calculated circadian power at each time point using the same 24 ± 4 h band as in the PER2::LUC and *Bmal1-ELuc* spectral analysis. This definition enables direct comparison between bioluminescence and qPCR-derived rhythmicity.

Phase dynamics and visualization. We estimated instantaneous phase (radians) along ridges of the time-frequency representation. Instead of plotting phase alone, we generated phase-weighted spectrograms, multiplying SST-CWT amplitude by its corresponding phase angle to highlight dominant oscillatory components with phase information. To improve visual clarity, colormap normalization and adaptive contrast scaling were applied using the maximum absolute value of each map. An illustration of this approach using simulated data is shown in **Fig. S6A**.

Circular phase plots. To track phase across development (E10.5, E12.5, E14.5, E16.5), we constructed circular phase plots based on the estimated instantaneous phase within the circadian range (20–28 h). For each embryonic cluster, the representative gene was plotted clockwise in a phase plot resembling a conventional clock, with 0 rad positioned at 12 o'clock. Non-representative genes from the same cluster were plotted with smaller, semi-transparent markers for comparison. The left semicircle was shaded to distinguish early vs late phases. Marker shape and color indicated cluster identity, and genes with circadian power ≥ 20% were outlined in black. To assess potential maternal-embryonic coordination, dual-radius phase plots were used: the inner ring showed embryonic cluster representatives, and the outer ring showed selected maternal genes. Maternal-embryonic pairs were connected with dotted lines when both exhibited circadian power ≥ 20% and their phase difference was < $\pi/2$ rad (≤ 6 h), indicating possible phase alignment.

Sliding-window correlation and network construction. To assess temporal coordination among maternal and embryonic genes, time series were padded by duplicating the first and last two points, and 5-timepoint sliding windows were applied. Pearson correlation matrices were computed for each window, generating a time-resolved sequence of correlations. Examples of dynamic correlation are shown in **Fig. S6B**. Networks were built in NetworkX (v2.5.1), with genes as nodes and edges weighted by average correlation within a developmental period. Edge consistency across periods was shown with solid lines, and changes in correlation sign with dashed lines. For maternal-embryo networks, only the top 30% strongest correlations were highlighted; the remainder were rendered in semi-transparent gray.

Results

PER2::LUC circadian oscillations emerge in the 4VCP before the SCN

The embryonic SCN is widely recognized as the earliest reported brain region to exhibit a detectable circadian rhythm, which emerges between E14.5 and E15.5 (Wreschnig et al., 2014; Carmona-Alcocer et al., 2018). To determine whether the SCN clock is unique at this developmental stage, we prepared

brain slices from E15.5 PER2::LUC$^{+/-}$ embryos and performed bioluminescence imaging for 5–7 days (**Fig. 1Aa**). Spectral analysis revealed two consistent loci with ~24 h periods, circadian power exceeding 30% (see Materials and Methods), and high RMS amplitude (**Fig. S4**). The ventral locus (white arrow) was LHX1-positive, confirming its identity as the SCN (VanDunk et al., 2011), whereas the posterior structure (red arrow) was TTR-positive, a known marker for the CP (Stauder et al., 1986) (**Fig. 1Cc**). When analysis was restricted to the SCN and 4VCP, a strong rhythm with a period between 20 and 28 h was detected (**Fig. 1Cd**). Notably, the pituitary gland also showed rhythmicity, but with a markedly lower RMS amplitude (**Fig. S4**).

To test whether the 4VCP begins to oscillate before the SCN, we repeated the experiment at E13.5 (**Fig. 1D**). We did not observe any circadian oscillation from ventral structures corresponding to SCN progenitors, consistent with previous reports (Wreschnig et al., 2014; Carmona-Alcocer et al., 2018) (**Fig. 1Db,Dd**). However, only the 4VCP (red arrow) exhibited a near-24 h rhythm with strong circadian power and high RMS amplitude (**Fig. 1Db** and **S4**), which we confirmed after restricting the analysis to the 4VCP (**Fig. 1Dd**). At E11.5, no significant circadian rhythm was detected in the 4VCP region in brain slices (**Fig. 1E**). Because the 4VCP in a slice could still be influenced by neighboring tissues, we asked whether the rhythm observed in E13.5 could originate from an endogenous 4VCP clock. Therefore, we dissected E13.5 4VCPs and recorded their bioluminescence *ex vivo* for 7 days (**Fig. 1F**). We found that the isolated 4VCP explant exhibited robust circadian rhythmicity at E13.5, with a mean circadian power of ~40%, well above the detection floor determined from blank luciferase medium (Blk, < 20%) (**Fig. 1Fb**).

To pinpoint the time of the clock emergence, we dissected 4VCPs from PER2::LUC embryos at embryonic stages beginning at E9.5, when the CSF compartment forms during neural tube closure (Chau et al., 2015), to postnatal stages. We recorded the 4VCP PER2::LUC bioluminescence from 110 embryos, with 3–11 embryos from at least 2–3 litters per stage, for 7 days with PMTs. The period, initially long and dispersed (37.08 ± 6.53 h at E10.5; n=17), converged toward 24 h by E11.5 (25.08 ± 0.88 h; n=15), when the first detectable oscillations appeared and circadian power exceeded 20% (31.21 ± 2.36% at E11.5; n=15; vs. 17.7 ± 1.69% at E10.5; n=17) (**Fig. 2A,C**). However, as seen in the head slice (**Fig. 1Ec**), these oscillations were weakly sustained, with low RMS amplitude. At E12.5, the oscillations persisted for the full 7-day recording, and their amplitude increased further at E13.5. The rhythm became fully circadian at E15.5 (24.47 ± 0.60 h; n=5), with high circadian power (50.96 ± 3.42%; n=5) relative to the 2-day window ceiling (~60%) (**Fig. 2A,C,D**).

We also used the *Bmal1-ELuc* reporter strain to characterize the molecular assembly of the embryonic circadian clock. A 24 h period in *Bmal1-ELuc* oscillation was observed from E13.5 to E14.5, approximately 2 days after the emergence of PER2 oscillations. From the sigmoidal fits to circadian power trajectories (see Materials and Methods), we estimated the emergence time T_e and found that PER2::LUC oscillations started to be circadian at E11.7 ± 0.14 *ex vivo*, whereas *Bmal1-ELuc* oscillations emerged at E13.52 ± 0.70 *ex vivo* (**Fig. 2D**). This result aligns with the sudden shift of the circadian power of PER2::LUC above 20% observed at E12.5 (**Fig. S5**). Because the circadian clock and developmental programs are intertwined, we mapped the embryonic 4VCP's developmental trajectory

404 by quantifying mRNA levels for stage-associated genes. For progenitor or stem cell markers, we
405 measured *Nanog* (stem cells), *Gli3* (neuroepithelium), *Wnt1* (roof-plate and CP epithelium progenitors)
406 (Awatramani et al., 2003; Hunter and Dymecki, 2007), and *Ki67* (proliferation). We compared these with
407 differentiation markers *Aqp1*, *Wnt5a*, *Ttr*, and *Otx2*, which are upregulated as the 4VCP matures
408 (Johansson et al., 2013; Lun et al., 2015b; Langford et al., 2020) (**Fig. 2E**). After normalizing each
409 transcript to its peak abundance between E9.5 and E16.5, we observed that progenitor markers
410 predominate from E9.5 to E12.5, whereas differentiation genes dominate thereafter (**Fig. 2E**).
411 Sigmoidal fits estimated the progenitor half-minimum at E13.63 ± 0.79 and the differentiation half-
412 maximum at E13.52 ± 0.20, marking a sharp transition that coincided with the *Bmal1-ELuc* T_e in the
413 4VCP (E13.52 ± 0.70), as anticipated from developmental maturation (Yagita, *et al*., 2024). By contrast,
414 PER2::LUC oscillations appear earlier and autonomously (E11.70 ± 0.14), and precede *Bmal1* and the
415 differentiation switch, an order that is atypical for a canonical TTFL (**Fig. 2G**).
416
417 Finally, we compared the emergence time of PER2::LUC rhythms across the brain and peripheral
418 organs in isolated explant culture. Among all tissues tested, the 4VCP was the first to become circadian,
419 preceding the LVCP (E12.37 ± 0.19), which develops later than the 4VCP (Lun et al., 2015b), and the
420 SCN (E14.21 ± 0.41), consistent with previous reports (Carmona-Alcocer et al., 2018). In the SCN, the
421 period approached 24 h at E14.5 (24.47 ± 2.35 h, *n*=7) and became fully circadian at E15.5 with high
422 circadian power (44.56 ± 2.48%, *n*=3). Peripheral organs emerged later in gestation and after the SCN
423 (liver: E14.53 ± 0.61; kidney: E15.08 ± 0.33) (**Fig. 2F,G**).
424
425 **Early-to-late circadian gene expression in the embryonic 4VCP**

426 Because mRNA and protein levels can be uncoupled during development (Umemura et al., 2017), we
427 assessed the emergence of circadian mRNA expression rhythms in the 4VCP. To capture circadian
428 variation, we sampled embryonic 4VCPs from 104 litters across E9–E16 at four circadian timepoints
429 (ZT2, ZT8, ZT14, ZT20) each embryonic day and performed RT-qPCR. We first compared the overall
430 mRNA levels of a specific gene set throughout development, and observed that at E9, the highest
431 transcript levels were for *Rora*, *Clock*, *Cry1*, and *Chrono*, rather than *Bmal1* and *Per1/2/3* (**Fig. 3A**).
432
433 We then clustered the transcripts according to their full temporal expression profiles across
434 development (**Fig. 3B**). Pairwise distances between expression profiles were computed using the
435 Pearson correlation, followed by hierarchical clustering. Four clusters emerged with distinct onset
436 patterns: early and sustained from E9.5 (Cluster 1: *Cry2*); inverted U-shaped, rising at ~E12.5 and
437 declining after ~E15.5 (Cluster 2: *Per2*, *Chrono*, *Rora*, *Rorc*); late-emerging at ~E13.5 (Cluster 3: *Per1*,
438 *Per3*, *Bmal1*, *Dbp*, *Clock*, *Rev-Erbβ*); and U-shaped, with an early onset at ~E9.5, a transient silence after
439 E11.5, and a rebound from ~E13.5 onward (Cluster 4: *Cry1*, *Rev-Erbα*). These clusters do not strictly align
440 with promoter motif architecture underlying the circadian transcriptional logic of the TTFL (Ukai-
441 Tadenuma et al., 2008; Takahashi, 2017). Notably, *Bmal1* and *Clock*, which act as drivers of the E-box
442 loop, belong to Cluster 3, and their baseline expression increases later than *Cry2* and *Per2* (**Fig. 3A**),
443 mirroring the onset-timing difference noted in *Bmal1-ELuc* and PER2::LUC reporter oscillations (**Fig.
444 2G**). In addition, *Per1* and *Per2*, both with glucocorticoid response elements (GREs) in their promoters

445 that can reset the clock in the CP (Liška et al., 2021), fall into two different clusters. These point to a
446 possibility that embryonic circadian gene expression in the 4VCP diverges from a simple TTFL-based
447 expectation.
448
449 We evaluated how circadian rhythms of each gene compared with the clusters, which are more
450 influenced by baseline changes across development, by quantifying circadian power using SST-CWT
451 analysis (Materials and Methods; **Fig. S7, S8A**). This analysis revealed that the strength of circadian
452 rhythmicity is unrelated to baseline expression patterns. Despite sustained expression, the Cluster 1
453 gene *Cry2* is circadian from E9 but rapidly loses rhythmicity; Cluster 2 shows heterogeneous behavior,
454 with *Per2* remaining below 20% circadian power; despite late increases in baseline expression, most
455 Cluster 3 genes become circadian around E11.5; and Cluster 4 genes remain circadian from E9 to E16
456 (**Fig. 3C**). To further validate our findings, we created phase-weighted power spectrograms of
457 representative transcripts (red), which visualize changes in dominant period and power together with
458 phase across cycles (**Fig. 3C**, lower panels). For several genes, including *Cry2, Chrono, Rora, Clock, Per1,*
459 and *Rev-erbβ*, we confirmed an initial circadian rhythm at E9–E10, which became indistinct around E13–
460 E14 and re-emerged at E15–E16 with an almost inverted phase (**Fig. S7, S8A**). Overall, most clock
461 genes in the embryonic 4VCP are transiently circadian before E16.5.
462
463 To better understand the establishment of the molecular clock and the dynamics between clusters, we
464 next compared the expression of the embryonic clock genes across development with the
465 representative gene of each cluster (**Fig. 3D**) and summarized the phase correlations in **Fig. 3E**. From
466 these correlative heat maps, we identified clusters whose correlations remained stable across time
467 (Cluster 2, 4 and claudin genes *Cldn2* and *Cldn11*) (**Fig. 3E**), with Cluster 2 and the claudins were
468 strongly positively correlated (**Fig. S8C**), and other clusters showing correlations that varied over
469 development. For the latter, three eras were apparent: E9–E11, E11–E13, and E13–E16. Although this
470 division suits most genes, it is especially clear for the dynamics between Cluster 3 (containing *Bmal1*)
471 and Cluster 4 (containing *Rev-Erbα*); while they are generally antiphasic (negatively correlated), they
472 become in-phase (positively correlated) between E11.5–E13.5 (**Fig. 3D, S8B**). The opposite trend can be
473 seen with Cluster 2 (*Rora*) and Cluster 3 (*Clock*); while generally positively correlated, they become
474 uncorrelated or negatively correlated around E11.5–E13.5 (**Fig. 3D, S8B, S8C**). Finally, we studied the
475 phase of expression to understand the origin of the change in correlation. Not only did the phase of
476 Cluster 3 and Cluster 4 change between E10.5 and E12.5, but the phases within each cluster also
477 became more homogeneous (**Fig. 3F**). By E16.5, we observed cluster polarization, with most positively
478 correlated and in-phase, whereas Cluster 4 was negatively correlated and antiphase to the others (**Fig.**
479 **3E, 3F**).
480
481 The absence of sustained PER2::LUC or *Bmal1-ELuc* rhythms in the embryonic 4VCP before E11.5–
482 E12.5 *ex vivo*, despite *Rev-Erbα* and *Cry2* being circadian *in vivo*, suggests that the early circadian gene
483 expression may depend on external inputs, such as maternal cues (Wong et al., 2022). We therefore
484 compared the expression profiles of selected clock genes in the 4VCP of 91 dams with the 4VCP of
485 PER2::LUC embryos. From hierarchical clustering, we identified 3 clusters of maternal clock genes,
486 which largely align with the gene classes, except for Cluster 1 which contains both E-box- and RRE-

driven genes: *Per2*, *Bmal1*, and *Cry1* (**Fig. 4A**). Surprisingly, in the maternal 4VCP, *Bmal1* and *Per2* expression, initially antiphasic, became in-phase around E11.5–E13.5 (**Fig. 4A, 4C, S10A**). SST-CWT analysis and circadian power estimation for each maternal gene (**Fig. S9**) showed all genes exhibited strong circadian power (**Fig. 4B, S9**).

To investigate how maternal signals might influence embryonic clock development, we examined temporal correlations between maternal and embryonic gene expression (**Fig. 4D, 4E**). We compared maternal *Per2*, *Bmal1*, and *Dbp* with representative genes from each embryonic cluster (**Fig. S10C**). We found that these correlations were not static but dynamically reorganized during development, revealing three distinct epochs that mirror the embryonic expression timeline, although less sharply defined. Before E11.5, when the embryonic clock is still immature and only Cluster 1 and 4 show circadian rhythmicity, maternal and embryonic *Bmal1* were largely uncorrelated. Cluster-specific patterns emerged nonetheless: Cluster 1 correlated positively with maternal *Bmal1*, whereas Cluster 4 correlated negatively with maternal *Dbp*, which are two maternal genes that are negatively correlated with each other (**Fig. 4C, 4E, S10B**). Between E11.5 and E13.5, as Clusters 2 and 3 acquire circadian rhythmicity, maternal-embryonic relations reorganized: correlation shifted away from maternal *Bmal1* and *Dbp* toward maternal *Per2*, suggesting that maternal *Per2* or associated pathway may help synchronize newly rhythmic components of the embryonic clock. This period might signify a major developmental phase transition, where the embryo's internal clock becomes more autonomous but still responsive to maternal signals. From E13.5 to E16.5, as most embryonic clusters acquired circadian rhythmicity (except Cluster 4), embryonic genes became negatively correlated with maternal *Bmal1*. Toward the end of this phase, correlation weakened substantially, consistent with increasing embryonic autonomy. Dual-radius phase plots further revealed a shift in maternal *Per2* and *Rora* expression around E12.5, while maternal *Bmal1* and *Dbp* remained relatively stable (**Fig. 4F**). This shift occurred precisely when maternal-embryonic correlation patterns reorganized, raising the possibility that some of maternal clock genes might undergo their own adjustments during this development window. Whether this reflects intrinsic maternal dynamics or embryo-evoked changes remains to be determined.

Taken together, these results indicate that maternal and embryonic clocks are coordinated, especially at E9.5–E11.5 when embryonic Clusters 1 and 4 are strongly correlated, and that the maternal clock appears to undergo a transient reorganization during the E11.5–E13.5 epoch. Notably, this epoch coincides with the functional maturation of the placenta, when maternal nutrient and oxygen supply to the embryonic circulation begins (Elmore et al., 2022). To test whether placental maturation contributes to this change in clock dynamics, we separated embryonic and maternal placentas and recorded PER2::LUC and *Bmal1-ELuc* bioluminescence *ex vivo*. As reported previously (Čečmanová et al., 2019), the embryonic placenta lacked autonomous circadian oscillations, whereas the maternal placenta exhibited robust rhythms with a transient mid-gestational attenuation (**Fig. 4G**). In the maternal placenta, circadian power of PER2::LUC and *Bmal1-ELuc* oscillations showed a mid-gestational nadir of ~20–30% at E15.3 ± 0.4 and E15.6 ± 0.6, respectively, estimated from inverted Gaussian fits. This dip occurs during E13–E15 and coincides with timing of increased activity of 11β-hydroxysteroid dehydrogenase type 2 (11β-HSD2) (E12.5-E16.5) (Salvante et al., 2017; Brown RW et al., 1996; Thompson *et al*., 2002), which inactivates glucocorticoids and is mainly active in the maternal

placenta, suggesting a potential endocrine gating mechanism that shields the embryo from the maternal influence (Astiz and Oster, 2021), although causality remains to be tested.

Temperature cycles can drive the embryonic 4VCP rhythmicity until E16.5

Because the circadian maternal core body temperature changes around E11.5 (Smarr et al., 2016) and because nutrition supply shifts from histiotrophic (yolk sac-based) to hemotrophic (blood-based), beginning at ~E10 and becoming fully functional by E12.5–E13.5 (Elmore et al., 2022), we hypothesized that small intrauterine temperature cycles could serve as a non-bloodborne driver of the nascent embryonic clock. During pregnancy, the maternal core-temperature rhythm amplitude dampens to ~1 °C, and to ~0.5 °C from around mid-gestation (Smarr et al., 2016). By contrast, many peripheral clocks *in vitro* require larger temperature cycles for entrainment (~4 °C, Brown et al., 2002; ~2.5 °C, Buhr et al., 2010; ~1.5 °C, Abraham et al., 2010), consistent with heat shock factor activation thresholds near ~2.5 °C (Brown and Rush, 1996; Buhr et al., 2010). If the embryonic 4VCP entrains to a 0.5 °C cycle, this would imply heightened phase sensitivity near onset, as expected for a system close to a SNIC threshold, rather than the higher-amplitude requirements typical of mature Hopf-type limit cycle oscillators.

We therefore tested temperature entrainment directly by recording PER2::LUC activity in cultured embryonic 4VCP explants. Since maternal body temperature at E6 varies between 37.5°C and 37°C (Wharfe et al., 2016), we applied 2 days at 37°C followed by 12 days of a 37–37.5°C (± 0.1 °C) cycle with a 26-h period to E14, E16, and E18 4VCP and lung explants (**Fig. 5A**). At E14, 4VCP PER2 rhythms entrained to the 26 h period temperature cycle, and at E16 they entrained after a brief transient, whereas at E18 the 0.5 °C temperature gradient did not entrain the 4VCP (**Fig. 5B**). Across all embryonic stages, the lung was entrained by the temperature cycle, possibly reflecting its prolonged structural maturation that continues postnatally. We applied the same protocol to the LVCP and SCN and found that the SCN remained entrainable at E18, which is plausible given that the SCN network is still immature at this stage (Bedont and Blackshaw, 2015), but the LVCP, like the 4VCP, was not (**Fig. S11A**). Together, these results indicate that small temperature cycles can influence the embryonic 4VCP through E16, whereas by E18, the oscillator exhibits reduced sensitivity to small temperature gradients and behaves more like a robust, limit cycle oscillator that maintains a stable rhythm under constant conditions.

Abrupt, SNIC-like onset and synchronization of clock emergence

A transition from a stable equilibrium to self-sustained oscillation is called a bifurcation. Single-cell circadian clocks are well described by robust limit cycles often modeled near a supercritical Hopf bifurcation, with amplitude that increases smoothly while the period remains near 24 h (Leloup and Goldbeter, 1999). By contrast, systems near a SNIC threshold show abrupt appearance of finite-amplitude oscillations, with very long initial periods that shorten toward ~24 h and can also display pronounced phase sensitivity to weak perturbations (Ermentrout, 1996). The bifurcation type can be probed by tracking how amplitude and period change over development. In our single-cell-resolution

PER2::LUC imaging data, we observe a sharply defined onset, with a long initial period and stepwise increase in single-cell amplitude (**Fig. 5C**), consistent with a SNIC-like onset near the birth of the circadian clock. Whole-tissue PER2::LUC luminometry likewise shows a long initial period that converges to ~24 h through development (**Fig. 2B**). The apparent linear increase in whole-tissue amplitude may partly reflect growth in 4VCP cell number across development (**Fig. S11B**).

At the population level, we observe an abrupt increase in synchronization at E14.5 (**Fig. 5D**), quantified by the Kuramoto order parameter, where 0 indicates the absence of synchronization and 1 indicates complete synchronization. The abrupt developmental shift is visible also in spatial phase distributions at day 4 in culture (**Fig. 5E**), reminiscent of abrupt synchronization emergence in the SCN (Carmona-Alcocer et al., 2018). These let us conclude that the clock emergence process at both single-cell and population levels are not gradual but discretely staged in developmental epochs.

Discussion

Our study identifies the embryonic choroid plexus as an early brain circadian clock that emerges before the SCN. Through PER2::LUC time lapse recording in 4VCP explant cultures, we found that circadian PER2 rhythms appear from E12.5, 2–3 days earlier than the central clock. We also observed staged assembly of the transcriptional clock circuit, with a delayed rise of *Bmal1* transcripts, coincident with the expression of the differentiation markers. Accordingly, we detected the postponed onset of *Bmal1-Eluc* oscillations *ex vivo* around E13.5.

When we performed circadian profiling of select transcripts across embryonic stages, we observed that 12 out of the 13 clock genes showed at least transient circadian expression patterns before E16.5 and displayed strong, developmentally shifting correlations with the maternal clock gene expression. Within a specific developmental window between E11.5 and E13.5, correlations among embryonic clock gene clusters were largely disrupted. This window coincides with placental maturation and the onset of maternal-fetal circulation. Before hemotrophic nutrition is established, the embryonic clock may be susceptible to blood-independent cues such as temperature, consistent with SNIC-like sensitivity near onset. After placental maturation, endocrine gating at the placenta may reduce maternal influence, enabling a developmental window for autonomous emergence and organization of circadian clocks in the embryo.

The CP, the first clock in the brain?

Contrary to the prevailing assumption that the SCN is the primary structure to be circadian in the mouse embryo because of its crucial role in adulthood, we found that the 4VCP clock emerges earlier than the SCN. In our study, the 4VCP is the earliest in the brain structure to display clear circadian rhythmicity, though our search is limited to select sagittal sections rather than across the entire 3D aspect of the embryonic brain. The 4VCP nevertheless has strong functional implications as the first clock, given our earlier demonstration that the adult 4VCP acts as a robust and influential oscillator

609 capable of entraining the SCN both *ex vivo* and *in vivo* (Myung et al., 2018). It is also notable that the
610 first three structures we identified as circadian before or around E15.5 are the CP, SCN, and pituitary
611 gland, which are all strategically positioned to regulate brain homeostasis, process external light cues,
612 and propagate outputs through endocrine pathways. Strikingly, these three structures also show the
613 strongest oscillations within the postnatal mouse brain (Myung et al., 2018).
614
615 The CSF-containing ventricles play a substantial role in early development; by E10.5–E11.5 the brain
616 ventricle volume is ≥10% of the head volume, substantially bathing the developing brain (Aristizábal et
617 al., 2013). This embryonic CSF is filled with morphogens and growth factors (Kaiser and Bryja, 2020;
618 Saunders et al., 2023; Lun et al., 2015a,b), mostly secreted from the CP. If the embryonic CP secretome
619 is released in a circadian manner, the neuroepithelium lining the large ventricles would receive
620 temporally patterned cues. Some of these inputs modulate transcription factors in neural progenitors
621 and influence fate decisions (Lamus et al., 2020; Lehtinen et al., 2011; Subashini et al., 2017). Although
622 not circadian, oscillations of basic-helix-loop-helix (bHLH) factors such as *Hes1*, *Ascl1*, and *Olig2*
623 promote cell proliferation, whereas sustained expression promotes cell differentiation (Imayoshi et al.,
624 2013). By inhibiting differentiation, the progenitor pool can expand before neurogenesis begins, a
625 prerequisite for reaching an appropriate number of both neurons and neural progenitors in the adult
626 stage (Caviness et al., 1995; Kriegstein and Alvarez-Buylla, 2009; Imayoshi and Kageyama, 2014). Other
627 factor-inducing pathways such as *Wnt*, *Hedgehog*, and *Notch* induce oscillatory patterns of target-gene
628 expression to regulate neural progenitor development (Imayoshi et al., 2014). This volume-transmission
629 from the CP is particularly important early in development, when synaptic circuits have yet to mature.
630 Synaptogenesis in the visual cortex, for instance, begins late in gestation and matures postnatally (Li et
631 al., 2010).
632
633 **Clock and CP differentiation**

634 The temporal convergence between 4VCP clock onset in culture and the start of the developmental
635 program, as well as the delay in clock onset between the 4VCP and the LVCP, illustrate the requirement
636 of differentiation for the clock to begin (Dan et al., 2020). These results agree with previous studies
637 showing that induced pluripotent stem cells (iPCSs), embryonic stem cells (ESCs), and pluripotent stem
638 cells (PSCs) lack a circadian clock, which emerges during differentiation (Yagita et al., 2010; Kowalska
639 et al., 2010; Kaneko et al., 2023; Umemura et al., 2017).
640
641 However, despite a progenitor profile marked by predominant markers such as *Gli3* and *Ki67* (**Fig. 2**),
642 we observed early circadian expression *in vivo* as early as E9.5 for *Cry2* when tissue is processed
643 immediately after sampling (**Fig. S7, S8**). This differs from whole-embryo analyses (Cao et al., 2022;
644 Dolatshad et al., 2010) and underscores the need to evaluate clock gene rhythmicity in a tissue-specific
645 manner. It is possible that some early rhythmic transcripts in the 4VCPs reflect maternally driven
646 activity. Challenges remain in determining the autonomous nature of such early gene oscillations as the
647 developing clock system may not conform to the adult model. For example, neonatal circadian clocks,
648 including the *Cry1*$^{-/-}$;*Cry2*$^{-/-}$ SCN, deviate from the behavior expected under the canonical TTFL model
649 (Ono et al., 2013).

Expression of *Per2* and *Bmal1* is typically antiphasic in the mature clock, since BMAL1-complexes drive *Per2* transcription, and after a delay due to translational and post-translational modifications, PER2-complexes repress transcription driven by BMAL1-complexes. In contrast, in our mRNA dataset, the two components do not co-emerge in the 4VCP, and in cultured explant recordings, *Bmal1-ELuc* starts circadian expression about ~2 days after PER2::LUC. This highlights the possibility that the very first oscillation of the embryonic clock may be independent of circadian *Bmal1* expression. It is plausible that other E-box activators operate during the early developmental stage, which do not need to be circadian themselves, as non-rhythmic *Bmal1* overexpression can lead to circadian expression of *Per2* (Liu et al., 2008) and *Bmal1* itself (Padlom et al., 2022). These features may relate to SNIC-like behavior, which most TTFL models do not predict. Regardless of the exact mechanism, this early clock could be physiologically important; for example, metabolic rhythms in glucose uptake have been observed in undifferentiated stem cells even when core clock genes appear arrhythmic (Paulose et al., 2012).

Entrainment of the late embryonic clock

Multiple lines of evidence indicate that a relatively autonomous clock operates by late gestation. In preterm infants, circadian-like rhythms in body temperature, heart rate, and rest-activity can be detectable in the NICU (Bueno et al., 2016; Mirmiran et al., 1990; Mirmiran and Kok, 1991; Govindan et al., 2024), consistent with a late-developing endogenous embryonic clock. Pups born from dams with late SCN lesions do not show inter-pup desynchrony, unlike litters from early SCN-lesioned dams (Davis and Gorski, 1988; Jud and Albrecht, 2006). In preterm infants, one study even demonstrated that the 24 h sleep-wake rhythm appears earlier in preterm than in full term babies (Guyer et al., 2015), although amplitude may be lower and phase may differ (e.g., inverted heart-rate rhythm; Govindan et al., 2024). Such phase differences could arise from changes in external zeitgebers such as feeding schedules. In mice, food restriction during and after pregnancy can shift offspring rhythms (Canaple et al., 2018). While ultradian temperature variation in the NICU generally does not seem to disrupt circadian development in infants born after mid-gestation (Thomas, 2001; Bueno et al., 2016; Mirmiran et al., 1990; Mirmiran and Kok, 1991), our data show that even when the 4VCP exhibits a strong rhythm at E16, it remains sensitive to weak temperature changes (0.5 °C), with reduced sensitivity by E18. These observations may help frame hypotheses about temperature-based care protocols customized to different stages of preterms.

Conclusion

The early emergence of the circadian clock in the 4VCP from E11.5 to E12.5 challenges the long-held view of the SCN as the central player of the circadian pacemaking in the mammalian brain and, by extension, as the locus of developmental onset. Our findings also reveal that the onset is a discrete, multi-stage process. We show that the *ex vivo* rhythm of the canonical transcriptional activator *Bmal1* appears later than that of *Per2*, suggesting that the embryonic clock is not established by the classic BMAL1:CLOCK feedback. Instead, qPCR analysis of the embryonic 4VCP uncovered non-canonical rhythmic expressions of *Chrono* and *Rev-Erbα* as early as E9.5. At the point of emergence, while mature

circadian oscillators are often described by a Hopf bifurcation, we find that this transition shows hallmarks of a SNIC bifurcation. Implications of these findings are twofold. First, the early clock in the 4VCP is best poised to guide the rhythms in other loci of the brain through the rhythmic secretion of factors into the CSF. Second, the internally multi-stage process and externally sudden emergence align with the idea that the circadian clock onset is a programmed developmental event, which provides a new framework for understanding the maternal-fetal clock interactions and the potential impact of their disruption. By characterizing the precise timing, locus, and mechanism of the brain's first clock, our work provides insights into early circadian homeostasis that are critically relevant to preterm and neonatal settings.

Acknowledgements

We thank Lilian Byer for critical reading of the manuscript. This work was supported by the National Science and Technology Council (NSTC) (109-2314-B-038-071, 109-2320-B-038-020, 110-2314-B-038-162, 110-2311-B-038-003, 111-2314-B-038-008, 112-2314-B-038-063, 113-2314-B-038-121, 114-2320-B-038-052-MY3, 114-2811-B-038-015) and the Higher Education Sprout Project of the Ministry of Education (MOE) in Taiwan.

References

Abraham U, Granada AE, Westermark PO, Heine M, Kramer A, Herzel H (2010). Coupling governs entrainment range of circadian clocks. *Mol Syst Biol*, 6:438.

Alonso MI, Martín C, Carnicero E, Bueno D, Gato A (2011). Cerebrospinal fluid control of neurogenesis induced by retinoic acid during early brain development. *Dev Dyn*, 240:1650–1659.

Alonso MI, Lamus F, Carnicero E, Moro JA, de la Mano A, Fernández JMF, Desmond ME, Gato A (2017). Embryonic cerebrospinal fluid increases neurogenic activity in the brain ventricular-subventricular zone of adult mice. *Front Neuroanat*, 11:124.

Aristizábal O, Mamou J, Ketterling JA, Turnbull DH (2013). High-Throughput, High-Frequency 3-D Ultrasound for in Utero Analysis of Embryonic Mouse Brain Development. *Ultrasound Med Biol*, *39*:2321–2332.

Astiz M, Oster H (2021). Feto-maternal crosstalk in the development of the circadian clock system. *Front Neurosci*, 14:631687.

Awatramani R, Soriano P, Rodriguez C, Mai JJ, Dymecki SM (2003). Cryptic boundaries in roof plate and choroid plexus identified by intersectional gene activation. *Nat Genet*, 35:70–75.

Balsalobre A, Damiola F, Schibler U (1998). A serum shock induces circadian gene expression in mammalian tissue culture cells. *Cell*, 93:929–937.

Battogtokh D, Tyson JJ (2018). Deciphering the dynamics of interlocked feedback loops in a model of the mammalian circadian clock. *Biophys J*, 115:2055–2066.

Bedont JL, Blackshaw S (2015). Constructing the suprachiasmatic nucleus: a watchmaker's perspective on the central clockworks. *Front Syst Neurosci*, 9:74.

Birecree E, King LE, Nanney LB (1991). Epidermal growth factor and its receptor in the developing human nervous system. *Dev Brain Res*, 60:145–154.

Brown IR, Rush SJ (1996). In vivo activation of neural heat shock transcription factor HSF1 by a physiologically relevant increase in body temperature. *J Neurosci Res*, 44:52-57.

Brown RW, Diaz R, Robson AC, Kotelevtsev YV, Mullins JJ, Kaufman MH, Seckl JR (1996). The ontogeny of 11 beta-hydroxysteroid dehydrogenase type 2 and mineralocorticoid receptor gene expression reveal intricate control of glucocorticoid action in development. *Endocrinology*, 137:794–797.

Brown SA, Zumbrunn G, Fleury-Olela F, Preitner N, Schibler U (2002). Rhythms of mammalian body temperature can sustain peripheral circadian clocks. *Curr Biol*, 12:1574–1583.

Bueno C, Menna-Barreto L (2016). Development of sleep/wake, activity and temperature rhythms in newborns maintained in a neonatal intensive care unit and the impact of feeding schedules. *Infant Behav Dev*, 44:21–28.

Bueno D, Parvas M, Nabiuni M, Miyan J (2020). Embryonic cerebrospinal fluid formation and regulation. *Semin Cell Dev Biol*, 102:3–12.

Buhr ED, Yoo SH, Takahashi JS (2010). Temperature as a universal resetting cue for mammalian circadian oscillators. *Science*, 330:379–385.

Cai C, Vandermeer B, Khurana R, Nerenberg K, Featherstone R, Sebastianski M, Davenport MH (2019). The impact of occupational shift work and working hours during pregnancy on health outcomes: a systematic review and meta-analysis. Am J Obstet Gynecol, 221:563–576.

Canaple L, Gréchez-Cassiau A, Delaunay F, Dkhissi-Benyahya O, Samarut J (2018). Maternal eating behavior is a major synchronizer of fetal and postnatal peripheral clocks in mice. *Cell Mol Life Sci*, *75*:3991–4005.

Cao X, Yan Y, Luo X, Yang X, Cui H, Yang Y, Li H (2022). Analyses of the circadian clock genes expression in whole embryos and maternal major tissues of mice. *J Mol Histol*, 53:473–482.

Carmona-Alcocer V, Abel JH, Sun TC, Petzold LR, Doyle FJ, Simms CL, Herzog ED (2018). Ontogeny of circadian rhythms and synchrony in the suprachiasmatic nucleus. *J Neurosci*, 38:1326–1334.

Caviness VS, Takahashi T, Nowakowski RS (1995). Numbers, time and neocortical neuronogenesis: a general developmental and evolutionary model. *Trends Neurosci*, 18:379–383.

Čečmanová V, Houdek P, Šuchmanová K, Sládek M, Sumová A (2019). Development and entrainment of the fetal clock in the suprachiasmatic nuclei: the role of glucocorticoids. *J Biol Rhythms*, 34:307–322.

Chau KF, Springel MW, Broadbelt KG, Park HY, Topal S, Lun MP, Mullan H, Maynard T, Steen H, LaMantia AS, Lehtinen MK (2015). Progressive differentiation and instructive capacities of amniotic fluid and cerebrospinal fluid proteomes following neural tube closure. *Dev Cell*, 35:789–802.

Courtney Y, Head JP, Dani N, Chechneva OV, Shipley FB, Zhang Y, Holtzman MJ, Sadegh C, Libermann TA, Lehtinen MK (2025). Choroid plexus apocrine secretion shapes CSF proteome during mouse brain development. *Nat Neurosci*, 28:1446–1459.

Dan H, Ruan T, Sampogna RV (2020). Circadian clock regulation of developmental time in the kidney. *Cell Rep*, 31:107661.

Daubechies I, Lu J, Wu HT (2011). Synchrosqueezed wavelet transforms: An empirical mode decomposition-like tool. *Appl Comput Harmon Anal*, 30:243–261.

Davari MH, Naghshineh E, Mostaghaci M, Mirmohammadi SJ, Bahaloo M, Jafari A, Mehrparvar AH (2018). Shift work effects and pregnancy outcome: A historical cohort study. *J Family Reprod Health*, 12:84–88.

Davis FC, Gorski RA (1988). Development of hamster circadian rhythms: role of the maternal suprachiasmatic nucleus. *J Comp Physiol A*, 162:601–610.

Dolatshad H, Cary AJ, Davis FC (2010). Differential expression of the circadian clock in maternal and embryonic tissues of mice. *PLoS ONE*, 5:e9855.

Dziegielewska KM, Ek J, Habgood MD, Saunders NR (2001). Development of the choroid plexus. *Microsc Res Tech*, 52:5–20.

Edelbo BL, Andreassen SN, Steffensen AB, MacAulay N (2023). Day-night fluctuations in choroid plexus transcriptomics and cerebrospinal fluid metabolomics. *PNAS Nexus*, 2:pgad262.

Elmore SA, Cochran RZ, Bolon B, Lubeck B, Mahler B, Sabio D, Ward JM (2022). Histology atlas of the developing mouse placenta. *Toxicol Pathol*, 50:60–117.

Ermentrout B (1996). Type I membranes, phase resetting curves, and synchrony. *Neural Comput*, 8:979–1001.

Gato A, Moro JA, Alonso MI, Bueno D, de La Mano A, Martín C (2005). Embryonic cerebrospinal fluid regulates neuroepithelial survival, proliferation, and neurogenesis in chick embryos. *Anat Rec A Discov Mol Cell Evol Biol*, 284:475–484.

Gato A, Desmond ME (2009). Why the embryo still matters: CSF and the neuroepithelium as interdependent regulators of embryonic brain growth, morphogenesis and histiogenesis. *Dev Biol*, 327:263–272.

789 Govindan RB, Andescavage NN, Basu S, Murnick J, Ngwa J, Galla JT, Kapse K, Limperopoulos C, du
790 Plessis A (2024). Circadian rhythm development in preterm infants: The role of postnatal versus
791 postmenstrual age. *Early Hum Dev*, 196:106084.

792 Guyer C, Huber R, Fontijn J, Bucher HU, Nicolai H, Werner H, Molinari L, Latal B, Jenni OG (2015). Very
793 preterm infants show earlier emergence of 24-hour sleep-wake rhythms compared to term infants.
794 *Early Hum Dev*, 91:37–42.

795 Hildyard JCW, Wells DJ, Piercy RJ (2022). Identification of qPCR reference genes suitable for
796 normalising gene expression in the developing mouse embryo. *Wellcome Open Res*, 6:197.

797 Huang X, Ketova T, Fleming JT, Wang H, Dey SK, Litingtung Y, Chiang C (2009). Sonic hedgehog
798 signaling regulates a novel epithelial progenitor domain of the hindbrain choroid plexus. *Development*,
799 136:2535–2543.

800 Hunter NL, Dymecki SM (2007). Molecularly and temporally separable lineages form the hindbrain roof
801 plate and contribute differentially to the choroid plexus. *Development*, 134:3449–3460.

802 Imayoshi I, Isomura A, Harima Y, Kawaguchi K, Kori H, Miyachi H, Fujiwara T, Ishidate F, Kageyama R
803 (2013). Oscillatory control of factors determining multipotency and fate in mouse neural progenitors.
804 *Science*, 342:1203–1208.

805 Imayoshi I, Kageyama R (2014). bHLH factors in self-renewal, multipotency, and fate choice of neural
806 progenitor cells. *Neuron*, 82:9–23.

807 Jia BZ, Qi Y, Wong-Campos JD, Megason SG, Cohen AE (2023). A bioelectrical phase transition patterns
808 the first vertebrate heartbeats. *Nature*, 622:149–155.

809 Johansson PA, Irmler M, Acampora D, Beckers J, Simeone A, Götz M (2013). The transcription factor
810 Otx2 regulates choroid plexus development and function. *Development*, 140:1055–1066.

811 Jud C, Albrecht U (2006). Circadian rhythms in murine pups develop in absence of a functional maternal
812 circadian clock. *J Biol Rhythms*, 21:149–154.

813 Kaiser K, Bryja V (2020). Choroid plexus: the orchestrator of long-range signalling within the CNS. *Int J*
814 *Mol Sci*, 21:4760.

815 Kaneko H, Kaitsuka T, Tomizawa K (2023). Artificial induction of circadian rhythm by combining
816 exogenous BMAL1 expression and polycomb repressive complex 2 inhibition in human induced
817 pluripotent stem cells. *Cell Mol Life Sci*, 80:200.

818 Kowalska E, Moriggi E, Bauer C, Dibner C, Brown SA (2010). The circadian clock starts ticking at a
819 developmentally early stage. *J Biol Rhythms*, 25:442–449.

820 Kriegstein A, Alvarez-Buylla A (2009). The glial nature of embryonic and adult neural stem cells. *Annu*
821 *Rev Neurosci*, 32:149–184.

822 Lamus F, Martín C, Carnicero E, Moro JA, Fernández JMF, Mano A, Gato Á, Alonso MI (2020). FGF2/EGF
823 contributes to brain neuroepithelial precursor proliferation and neurogenesis in rat embryos: the
824 involvement of embryonic cerebrospinal fluid. *Dev Dyn*, 249:141–153.

825 Landgraf D, Koch CE, Oster H, Alvarez-Bolado G, Pombal MA (2014). Embryonic development of
826 circadian clocks in the mammalian suprachiasmatic nuclei. *Front Neuroanat,* 8:143.

827 Langford MB, O'Leary CJ, Veeraval L, White A, Lanoue V, Cooper HM (2020). WNT5a regulates
828 epithelial morphogenesis in the developing choroid plexus. *Cereb Cortex*, 30:3617–3631.

829 Lehtinen MK, Zappaterra MW, Chen X, Yang YJ, Hill AD, Lun M, Maynard T, Gonzalez D, Kim S, Ye P,
830 D'Ercole AJ, Wong ET, LaMantia AS, Walsh CA (2011). The cerebrospinal fluid provides a proliferative
831 niche for neural progenitor cells. *Neuron*, 69:893–905.

832 Li M, Cui Z, Niu Y, Liu B, Fan W, Yu D, Deng J (2010). Synaptogenesis in the developing mouse visual
833 cortex. *Brain Res Bull*, 81:107–113.

834 Liu AC, Tran HG, Zhang EE, Priest AA, Welsh DK, Kay SA (2008). Redundant function of REV-ERBα and
835 β and non-essential role for Bmal1 cycling in transcriptional regulation of intracellular circadian
836 rhythms. *PLoS Ge*net, 4:e1000023.

837 Liška K, Sládek M, Čečmanová V, Sumová A (2021). Glucocorticoids reset circadian clock in choroid
838 plexus via period genes. *J Endocrinol*, 248:155–166.

839 Lun MP, Johnson MB, Broadbelt KG, Watanabe M, Kang YJ, Chau KF, Springel MW, Malesz A, Sousa
840 AMM, Pletikos M, Adelita T, Calicchio ML, Zhang Y, Holtzman MJ, Lidov HGW, Sestan N, Steen H,
841 Monuki ES, Lehtinen MK (2015a). Spatially heterogeneous choroid plexus transcriptomes encode
842 positional identity and contribute to regional CSF production. *J Neurosci*, 35:4903–4916.

843 Lun MP, Monuki ES, Lehtinen MK (2015b). Development and functions of the choroid plexus-
844 cerebrospinal fluid system. *Nat Rev Neurosci*, 16:445–457.

845 Maeda Y, Muro M, Shono M, Shono H, Iwasaka T (2006). Diurnal rhythms in fetal heart rate baseline
846 and sustained fetal tachycardia in twin pregnancy. *Early Hum Dev*, 82:637–644.

847 Martín C, Bueno D, Alonso MI, Moro JA, Callejo S, Parada C, Martín P, Carnicero E, Gato A (2006). FGF2
848 plays a key role in embryonic cerebrospinal fluid trophic properties over chick embryo neuroepithelial
849 stem cells. *Dev Biol,* 297:402–416.

850 Martin C, Alonso MI, Santiago C, Moro JA, de la Mano A, Carretero R, Gato A (2009). Early embryonic
851 brain development in rats requires the trophic influence of cerebrospinal fluid. *Int J Dev Neurosci*,
852 27:733–740.

853 Mirmiran M, Kok JH, de Kleine MJK, Koppe JG, Overdijk J, Witting W (1990). Circadian rhythms in
854 preterm infants: a preliminary study. *Early Hum Dev*, 23:139–146.

855 Mirmiran M, Kok JH (1991). Circadian rhythms in early human development. *Early Hum Dev*, 26:121–
856 128.

857 Miyan JA, Nabiyouni M, Zendah M (2003). Development of the brain: a vital role for cerebrospinal fluid.
858 *Can J Physiol Pharmacol*, 81:317–328.

859 Murayama Y, Kori H, Oshima C, Kondo T, Iwasaki H, Ito H (2017). Low temperature nullifies the
860 circadian clock in cyanobacteria through Hopf bifurcation. *Proc Natl Acad Sci USA*, 114:5641–5646.

861 Myung J, Hong S, Hatanaka F, Nakajima Y, De Schutter E, Takumi T (2012). Period coding of Bmal1
862 oscillators in the suprachiasmatic nucleus. *J Neurosci*, 32:8900–8918.

863 Myung J, Hong S, DeWoskin D, De Schutter E, Forger DB, Takumi T (2015). GABA-mediated repulsive
864 coupling between circadian clock neurons in the SCN encodes seasonal time. *Proc Natl Acad Sci USA*,
865 112:E3920–E3929.

866 Myung J, Schmal C, Hong S, Tsukizawa Y, Rose P, Zhang Y, Holtzman MJ, De Schutter E, Herzel H,
867 Takumi T (2018). The choroid plexus is an important circadian clock component. *Nat Commun*, 9:1–13.

868 Myung J (2024). Enhancing bioluminescence imaging of cultured tissue explants using optical
869 telecompression. *Sensors*, 24:6041.

870 Myung J, Vitet H, Truong VH, Ananthasubramaniam B (2025). The role of the multiplicity of circadian
871 clocks in mammalian systems. *Sleep Med*, 131:106518.

872 Nakajima Y, Yamazaki T, Nishii S, Noguchi T, Hoshino H, Niwa K, Viviani VR, Ohmiya Y (2010).
873 Enhanced beetle luciferase for high-resolution bioluminescence imaging. *PLoS ONE*, 5:e10011.

874 Oates AC, Morelli LG, Ares S (2012). Patterning embryos with oscillations: structure, function and
875 dynamics of the vertebrate segmentation clock. *Development*, 139:625–639.

876 Ono D, Honma S, Honma KI (2013). Cryptochromes are critical for the development of coherent
877 circadian rhythms in the mouse suprachiasmatic nucleus. *Nat Commun*, 4:1666.

878 Padlom A, Ono D, Hamashima R, Furukawa Y, Yoshimura T, Nishiwaki-Ohkawa T (2022). Level of
879 constitutively expressed BMAL1 affects the robustness of circadian oscillations. *Sci Rep*, 12:19519.

880 Parada C, Escolà-Gil JC, Bueno D (2008). Low-density lipoproteins from embryonic cerebrospinal fluid
881 are required for neural differentiation. *J Neurosci Res*, 86:2674–2684.

882 Parvas M, Parada C, Bueno D (2008). A blood-CSF barrier function controls embryonic CSF protein
883 composition and homeostasis during early CNS development. *Dev Biol*, 321:51–63.

884 Paulose JK, Rucker EB, Cassone VM (2012). Toward the beginning of time: Circadian rhythms in
885 metabolism precede rhythms in clock gene expression in mouse embryonic stem cells. *PLoS ONE*,
886 7:e49555.

Salvante KG, Milano K, Kliman HJ, Nepomnaschy PA (2017). Placental 11 β-hydroxysteroid dehydrogenase type 2 (11β-HSD2) expression very early during human pregnancy. *J Dev Orig Health Dis*, 8:149–154

Saunders NR, Dziegielewska KM, Fame RM, Lehtinen MK, Liddelow SA (2023). The choroid plexus: A missing link in our understanding of brain development and function. *Physiol Rev*, 103:919–956.

Serón-Ferré M, Mendez N, Abarzua-Catalan L, Vilches N, Valenzuela FJ, Reynolds HE, Llanos AJ, Rojas A, Valenzuela GJ, Torres-Farfan C (2012). Circadian rhythms in the fetus. *Mol Cell Endocrinol*, 349:68–75.

Smarr BL, Zucker I, Kriegsfeld LJ (2016). Detection of successful and unsuccessful pregnancies in mice within hours of pairing through frequency analysis of high temporal resolution core body temperature data. *PLoS ONE*, 11:e0160127.

Stauder AJ, Dickson PW, Aldred AR, Schreiber G, Mendelsohn FA, Hudson P (1986). Synthesis of transthyretin (pre-albumin) mRNA in choroid plexus epithelial cells, localized by in situ hybridization in rat brain. *J Histochem Cytochem*, 34:949–952.

Strogatz SH (2024). *Nonlinear Dynamics and Chaos: With Applications to Physics, Biology, Chemistry, and Engineering*. 3rd ed. New York: Chapman & Hall/CRC.

Subashini C, Dhanesh SB, Chen CM, Riya PA, Meera V, Divya TS, Kuruvilla R, Buttler K, James J (2017). Wnt5a is a crucial regulator of neurogenesis during cerebellum development. *Sci Rep*, 7:42523.

Takahashi JS (2017). Transcriptional architecture of the mammalian circadian clock. *Nat Rev Genet*, 18:164–179.

Thomas KA (2001). Biological rhythm development in preterm infants: Does health status influence body temperature circadian rhythm? *Res Nurs Health*, 24:170–180.

Thompson, A., Han, V. K. M., & Yang, K. (2002). Spatial and temporal patterns of expression of 11β-hydroxysteroid dehydrogenase types 1 and 2 messenger RNA and glucocorticoid receptor protein in the murine placenta and uterus during late pregnancy. *Biol Repro*, 67:1708–1718.

Truong VH, Myung J (2023). LocoBox: Modular Hardware and Open-Source Software for Circadian Entrainment and Behavioral Monitoring in Home Cages. *Sensors*, 23:9469.

Ukai-Tadenuma M, Kasukawa T, Ueda HR (2008). Proof-by-synthesis of the transcriptional logic of mammalian circadian clocks. *Nat Cell Biol*, 10:1154–1163.

Umemura Y, Koike N, Ohashi M, Tsuchiya Y, Meng QJ, Minami Y, Hara M, Hisatomi M, Yagita K (2017). Involvement of posttranscriptional regulation of Clock in the emergence of circadian clock oscillation during mouse development. *Proc Natl Acad Sci USA*, 114:E7479–E7488.

VanDunk C, Hunter LA, Gray PA (2011). Development, maturation, and necessity of transcription factors in the mouse suprachiasmatic nucleus. *J Neurosci*, 31:6457–6467.

Wharfe MD, Mark PJ, Wyrwoll CS, Smith JT, Yap C, Clarke MW, Waddell BJ (2016). Pregnancy-induced adaptations of the central circadian clock and maternal glucocorticoids. *J Endocrinol*, 228:135–147.

Wong SD, Wright KP, Spencer RL, Vetter C, Hicks LM, Jenni OG, LeBourgeois MK (2022). Development of the circadian system in early life: maternal and environmental factors. *J Physiol Anthropol*, 41:22.

Wreschnig D, Dolatshad H, Davis FC (2014). Embryonic development of circadian oscillations in the mouse hypothalamus. *J Biol Rhythms*, 29:299–310.

Yagita K (2024). Emergence of the circadian clock oscillation during the developmental process in mammals. *Curr Opin Genet Dev*, 84:102152.

Yagita K, Horie K, Koinuma S, Nakamura W, Yamanaka I, Urasaki A, Shigeyoshi Y, Kawakami K, Shimada S, Takeda J, Uchiyama Y (2010). Development of the circadian oscillator during differentiation of mouse embryonic stem cells in vitro. *Proc Natl Acad Sci USA*, 107:3846–3851.

Yamazaki S, Numano R, Abe M, Hida A, Takahashi RI, Ueda M, Block GD, Sakaki Y, Menaker M, Tei H (2000). Resetting central and peripheral circadian oscillators in transgenic rats. *Science*, 288:682–685.

Yoo SH, Yamazaki S, Lowrey PL, Shimomura K, Ko CH, Buhr ED, Siepka SM, Hong HK, Oh WJ, Yoo OJ, Menaker M, Takahashi JS (2004). PERIOD2::LUCIFERASE real-time reporting of circadian dynamics reveals persistent circadian oscillations in mouse peripheral tissues. *Proc Natl Acad Sci USA*, 101:5339–5346.

Zappaterra MW, Lehtinen MK (2012). The cerebrospinal fluid: Regulator of neurogenesis, behavior, and beyond. *Cell Mol Life Sci*, 69:2863–2878.

1

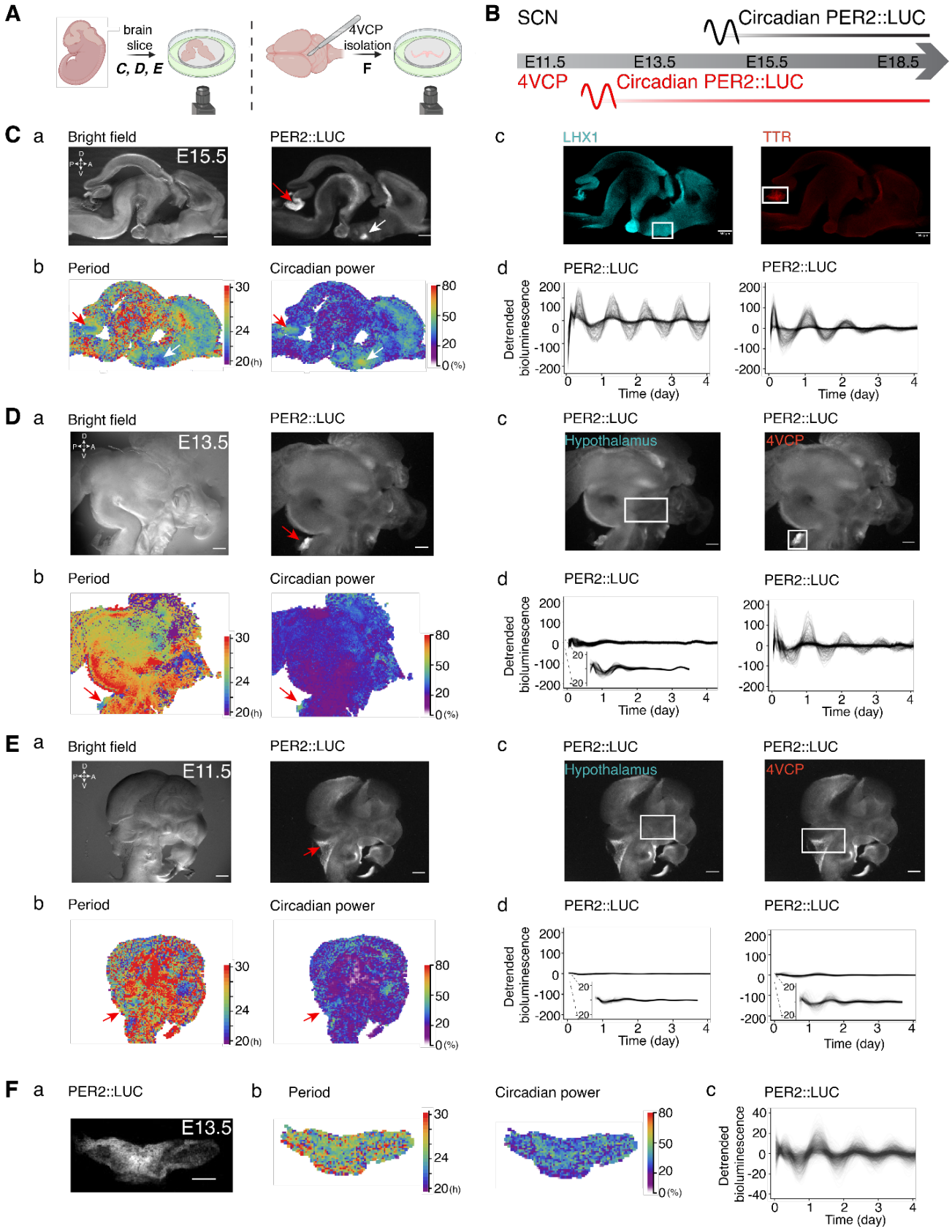
A
brain slice
C, D, E
4VCP isolation
F
B
SCN
Circadian PER2::LUC
E11.5
E13.5
E15.5
E18.5
4VCP
Circadian PER2::LUC
C a
Bright field
E15.5
PER2::LUC
b
Period
Circadian power
c
LHX1
TTR
d
PER2::LUC
Detrended bioluminescence
Time (day)
D a
E13.5
b
c
Hypothalamus
4VCP
d
E a
E11.5
b
c
d
F a
PER2::LUC
E13.5
b
Period
Circadian power
c
PER2::LUC
Detrended bioluminescence
Time (day)

Figure 1. The 4VCP is circadian before the SCN in the mouse embryonic brain. (**A**) Schematic of the protocol used for recording PER2::LUC bioluminescence from embryonic brain or head slices (left) or from the isolated 4VCP (right). (**B**) Illustration summarizing the finding that the 4VCP is circadian earlier than the SCN in the mouse embryo. (**C**) **a**: Bright field and PER2::LUC images of the bioluminescence obtained from a PER2::LUC E15.5 brain slice. **b**: Analysis of the recording showing the period (left) and the circadian power (right). **c**: Images of immunofluorescence of LHX1 (left) and TTR (right) after brain clearing **d**: Detrended time series of PER2::LUC bioluminescence from the areas indicated by the white boxes in **c.** (**D**) **a**: Bright field and PER2::LUC images of the bioluminescence obtained from a PER2::LUC E13.5 head slice. **b**: Analysis of the recording showing the period (left) and the circadian power (right). **c**: PER2::LUC images with white boxes indicating the putative hypothalamus (left) and 4VCP (right). **d**: Detrended time series of PER2::LUC bioluminescence from the areas indicated by the white boxes in **c.** (**E**) **a**: Bright field and PER2::LUC images of the bioluminescence obtained from a PER2::LUC E11.5 head slice. **b**: Analysis of the recording showing the period (left) and the circadian power (right). **c**: PER2::LUC images with white boxes indicating the putative hypothalamus (left) and 4VCP (right). **d**: Detrended time series of PER2::LUC bioluminescence from the areas indicated by the white boxes in **c.** (**F**) **a**: PER2::LUC image of the bioluminescence obtained from a PER2::LUC E13.5 isolated 4VCP. **b**: Analysis of the recording showing the period (left) and the circadian power (right). **c**: Detrended time series of the recording. Scale bar: 500 μm. Red arrows indicate 4VCP and white arrows indicate SCN.

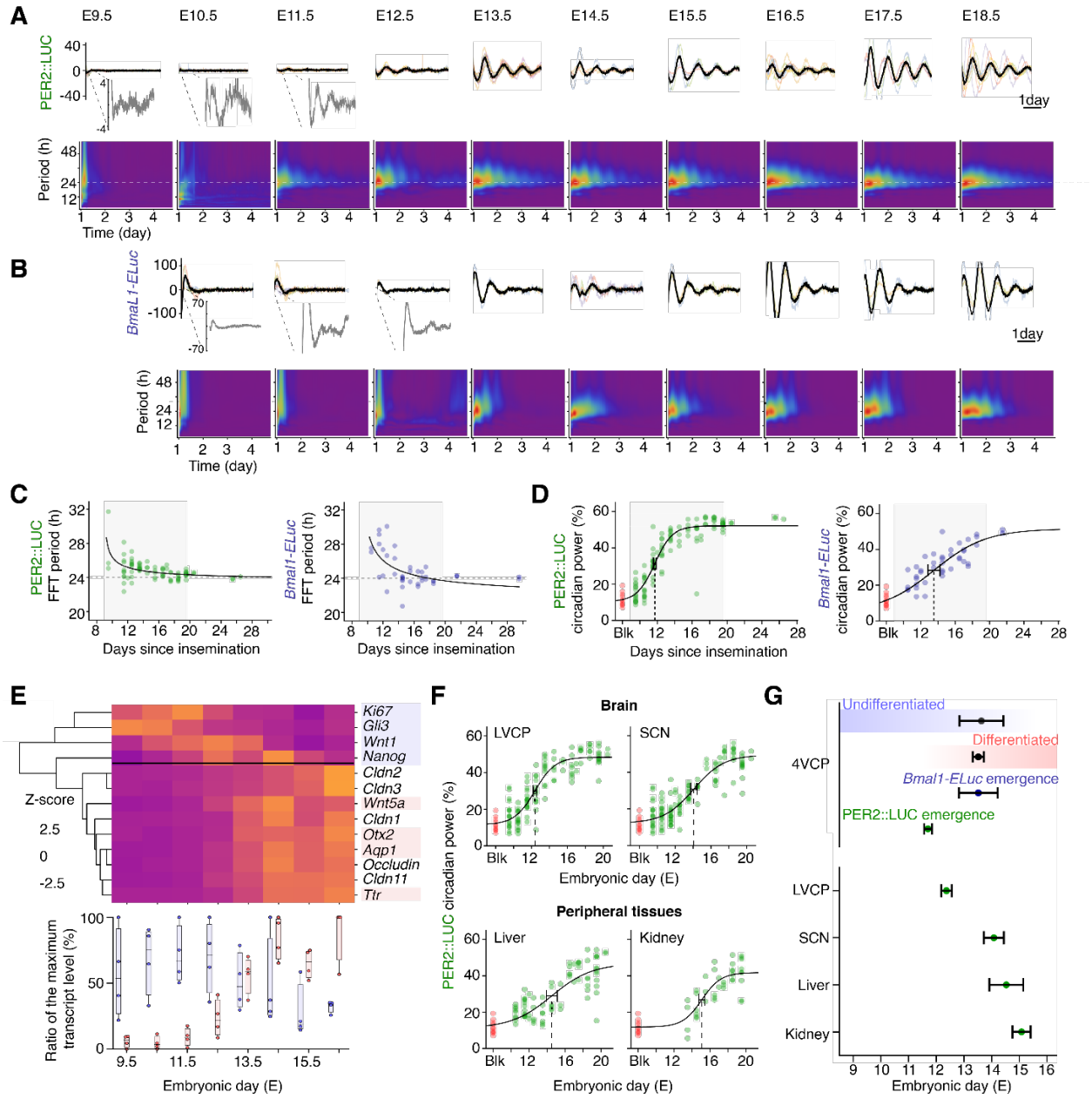

Figure 2. The 4VCP clock emerges at E11.5–E12.5, preceding the LVCP and the SCN and coinciding with the onset of 4VCP differentiation. (**A**) Individual (thin colored) and mean (black) detrended traces (top) and spectrograms (bottom) of PER2::LUC bioluminescence recorded from embryonic 4VCP from E9.5 to E18.5. Zoom-in insets highlight low amplitude rhythms. (**B**) Individual (thin colored) and mean (black) detrended traces (top) and spectrograms (bottom) of *Bmal1-ELuc* bioluminescence recorded from embryonic 4VCP from E10.5 to E18.5. Zoom-in insets highlight low amplitude rhythms. (**C**) Period scatter plots for PER2::LUC (left) and *Bmal1-ELuc* (right) with $1/\sqrt{(t - t_0)}$ fits (consistent with SNIC). (**D**) Circadian power scatter plots for PER2::LUC (left) and *Bmal1-ELuc* (right) with sigmoid fits versus embryonic age; emergence times (T_e) were E11.70 ± 0.14 and E13.52 ± 0.70, respectively (best fit estimate ± SE). (**E**) Heat map of the clustering of genes characterizing the developmental state (top) and comparison of transcript levels of stem cell and progenitor markers

(blue), differentiation markers (red) in the 4VCP across embryonic stages, normalized to the highest expression between E9.5 and E16.5 (down). Each data point represents a mean of 5–15 litters (3–11 embryos per litter). Whiskers plot displays the minimum to maximum values, the 25th and 75th percentile and the median. (**F**) Developmental trajectories of circadian power for PER2::LUC oscillation in the LVCP and the SCN (upper panels) and liver and kidney (lower panels), overlaid with sigmoidal fits. (**G**) Comparison of the half-maximal times for progenitor markers (E13.63 ± 0.79), differentiation markers (E13.52 ± 0.20), emergence time of *Bmal1-ELuc* and PER2::LUC oscillation in the 4VCP, and of the PER2::LUC emergence time for each tissue.

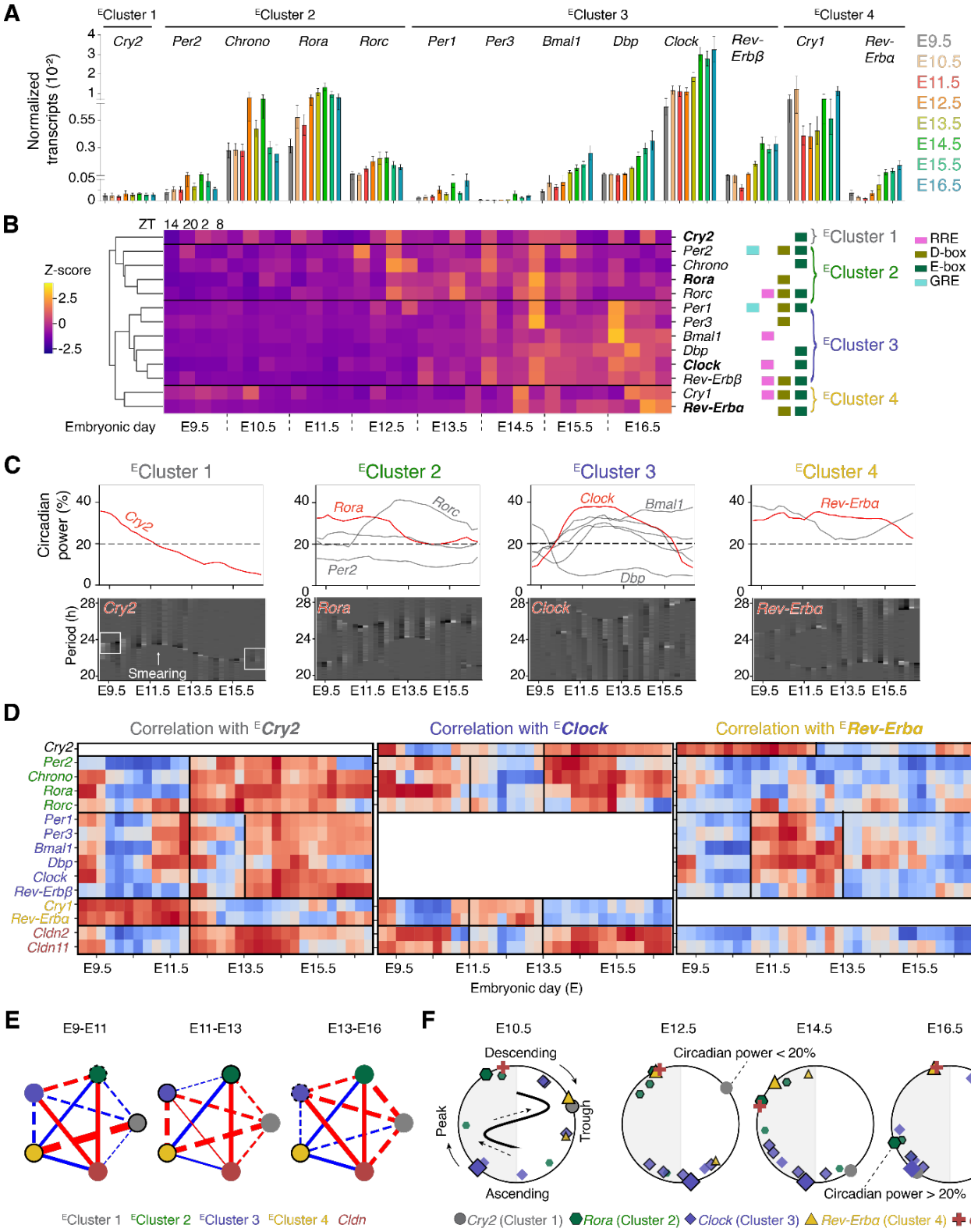

Figure 3. Expression patterns of clock genes in the embryonic 4VCP. (**A**) Absolute mRNA levels of clock gene transcripts across embryonic stages E9 to E16. Bars show the mean ± SEM of 8–20

litters, each litter containing 3–11 embryos. (**B**) Hierarchical clustering and heat map of mRNA Z-scores across embryonic stages and ZT for the clock genes. Each data point represents the mean of 2–5 litters, each with 3–11 embryos. (**C**) Circadian power for each embryonic clock gene, grouped by cluster (top); the representative gene of each cluster is plotted in red. Circadian phase-weighted power spectrogram across embryonic days for the representative gene of each cluster (bottom); the left white box marks the initial phase and the right white box marks the shifted phase in the end. (**D**) Heat maps of pairwise correlations between each embryonic gene and *Cry2* (left), *Clock* (middle) and *Rev-Erbα* (right), the representative genes. (**E**) Temporal correlation networks of embryonic genes. Nodes denote gene clusters. Edge color and width encode the sign and absolute value of the average Pearson within the specified developmental window, respectively (blue negative, red positive, greater width indicates larger magnitude). Solid edges indicate correlations with consistent signs across stages; dashed edges indicate a sign change across stages. Black outlines indicate genes with circadian power ≥ 20%. (**F**) Circular phase plots of embryonic gene expression across developmental stages. Each phase plot has 0 rad at 12 o'clock and increases clockwise. Representative genes are shown with larger opaque markers; non-representative genes are smaller and semi-transparent. The left-half shading indicates earlier phases. Marker shape and color indicate cluster membership; bold outlines highlight genes with circadian power ≥ 20%.

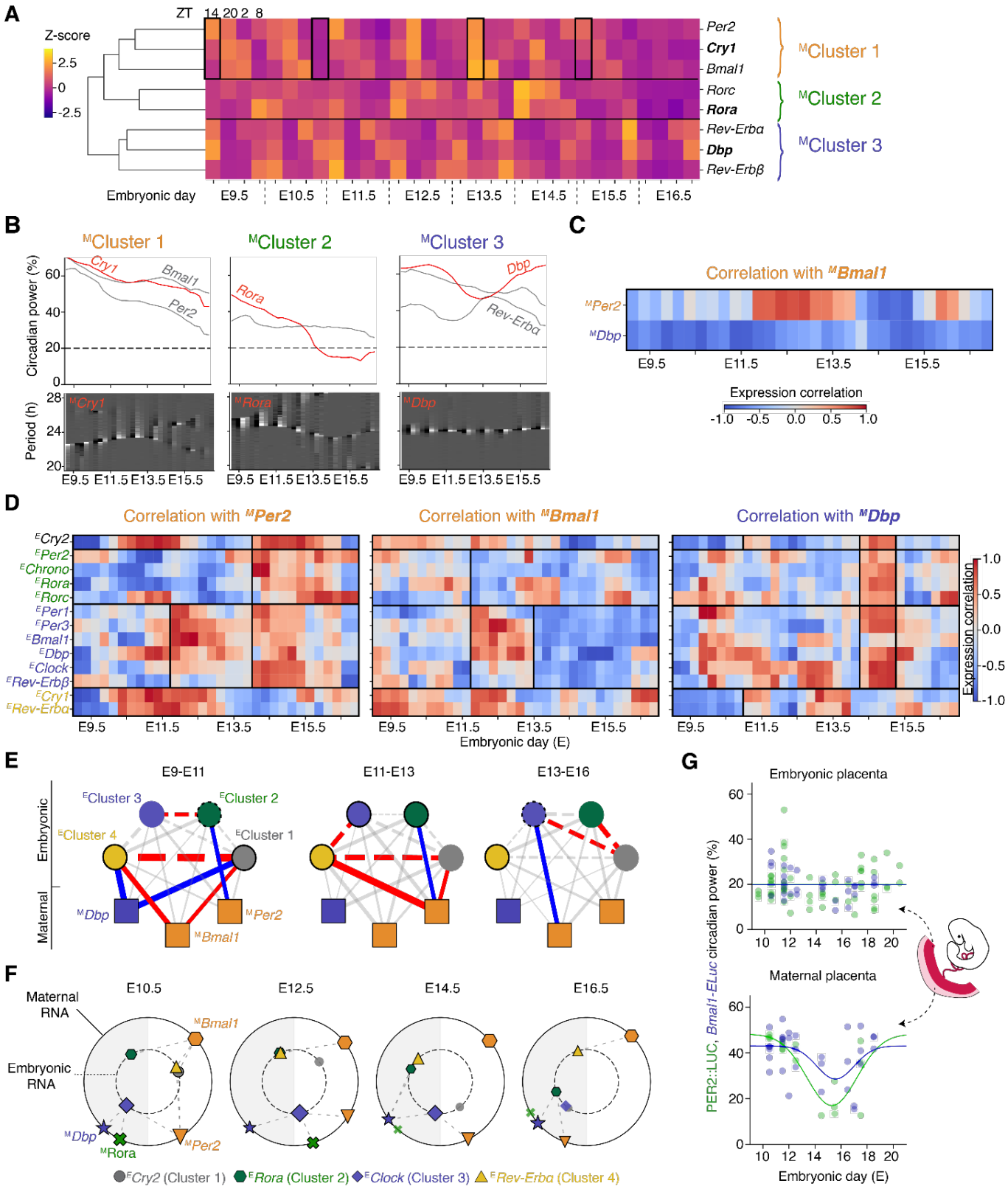

Figure 4. Correlations between maternal and embryonic gene expression vary with embryonic development. (**A**) Hierarchical clustering and heat map of the mRNA Z-scores across embryonic

stages and ZT for maternal clock genes. Each data point represents the mean of 2-3 dams. (**B**) Circadian power for each maternal clock gene per cluster (top). The representative gene of each cluster is shown in red. Circadian phase-weighted power spectrogram across embryonic days for the representative gene of each maternal gene cluster (bottom). (**C**) Heat map of the correlation of maternal *Per2* and *Dbp* with *Bmal1.* (**D**) Heat map of the correlation of each embryonic gene with maternal *Per2* (left), *Bmal1* (middle), and *Dbp* (right). (**E**) Temporal correlation networks of maternal-embryonic gene expression correlations. Nodes colored by embryonic clusters; edges show average Pearson correlation (red positive, blue negative, thickness magnitude). Solid edges indicate consistent sign, dashed indicate changing sign. Black outlines mark genes with circadian power ≥ 20%. Only the top 30% strongest correlations are highlighted; others are semi-transparent gray. (**F**) Dual-radius phase plots of maternal and embryonic gene expression. Inner ring, embryonic cluster representatives; outer ring, selected maternal genes. Maternal-embryonic pairs are connected with dotted lines when both exhibit circadian power ≥ 20% and their phase difference is $< \pi/2$ rad (≤ 6 h). (**G**) PER2::LUC and *Bmal1-ELuc* circadian power in the embryonic (top, dark pink) and maternal (down, light pink) placenta from 97 embryonic and 47 maternal placentas from E10.5 to E18.5.

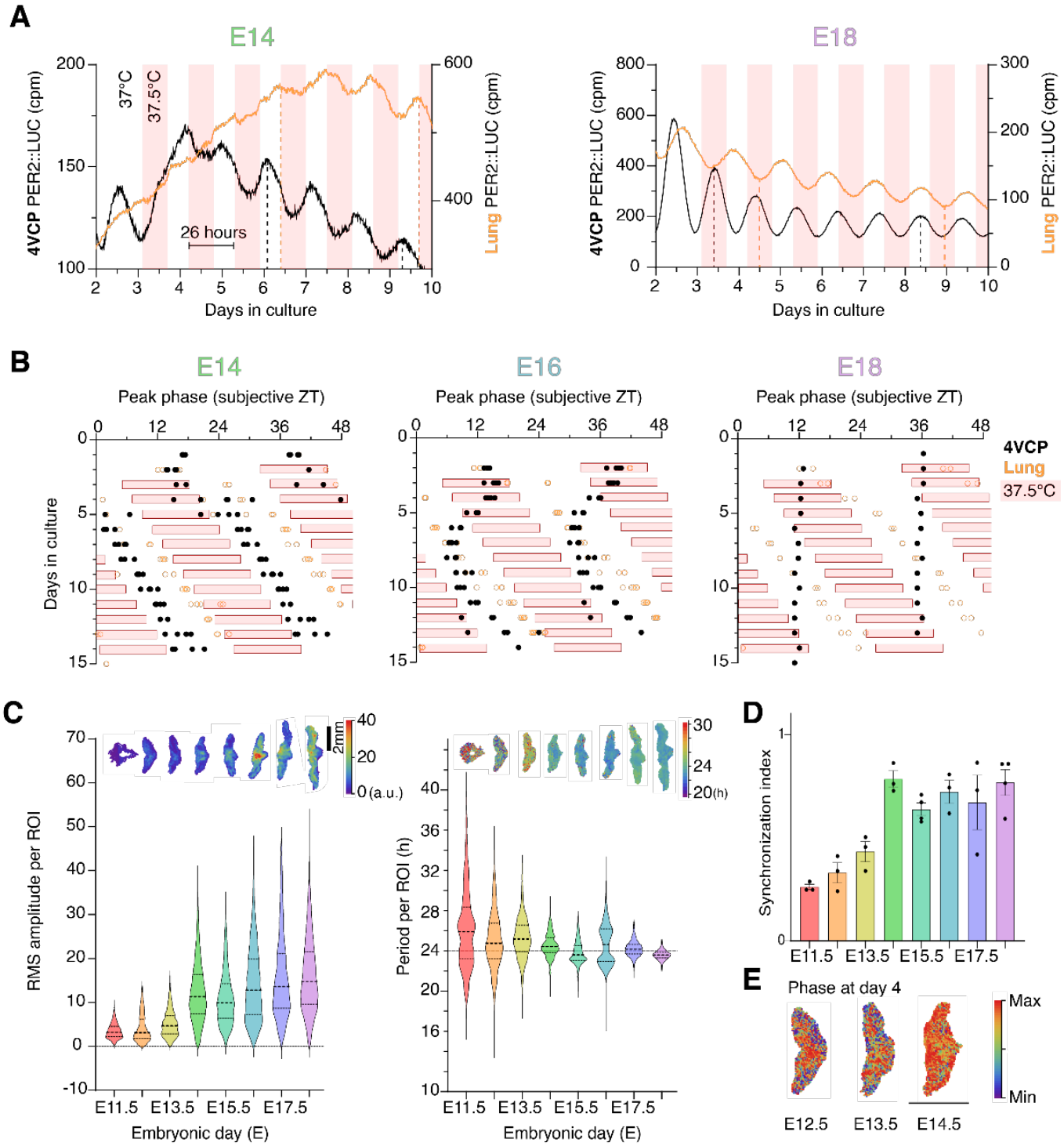

Figure 5. E14 and E16 4VCP, but not E18 4VCP, are driven to a 26-h period temperature cycle. (**A**) Raw PER2::LUC time series from 4VCP (black) and lung (orange) explanted at E14 (left) and E18 (right) for 12 days with a 0.5°C square-wave cycle (26 h period) after 2 days at 37 °C. Red bars indicate the 37.5 °C epochs. (**B**) Double-plots of the peak phase of PER2::LUC time series from 1–4 embryonic 4VCPs and lungs at E14 (left), E16 (middle), and E18 (right). Red bars indicate the 37.5°C epochs. (**C**)

Violin plots showing amplitude (left) and period (right) per ROI in embryonic 4VCP across embryonic stages from E11.5 to E18.5 (579–2,787 cells from 3–4 4VCPs from 2–3 litters). The dotted line represents the median and the black lines represent the quartiles. Representative maps showing the single-cell level amplitude (top left) and period (top right) across stages. (**D**) Bar plot showing the mean ± SEM synchronization index in embryonic 4VCP overlaid with scatter plots showing individual 4VCP data across stages (579–2,787 cells from 3–4 4VCPs from 2–3 litters). (**E**) Representative 4VCP maps showing the normalized phase after 4 days in culture at E12.5, E13.5 and E14.5. Scale bar: 2 mm.